

Automated asteroseismic peak detections

A. García Saravia Ortiz de Montellano^{1,2*}, S. Hekker^{1,2}, N. Themeßl^{1,2}

¹Max-Planck-Institut für Sonnensystemforschung, Justus-von-Liebig-Weg 3, 37077 Göttingen, Germany

²Stellar Astrophysics Centre, Department of Physics and Astronomy, Aarhus University, Ny Munkegade 120, DK-8000 Aarhus C, Denmark

Accepted XXX. Received YYY; in original form ZZZ

ABSTRACT

Space observatories such as *Kepler* have provided data that can potentially revolutionise our understanding of stars. Through detailed asteroseismic analyses we are capable of determining fundamental stellar parameters and reveal the stellar internal structure with unprecedented accuracy. However, such detailed analyses, known as peak bagging, have so far been obtained for only a small percentage of the observed stars while most of the scientific potential of the available data remains unexplored. One of the major challenges in peak bagging is identifying how many solar-like oscillation modes are visible in a power density spectrum. Identification of oscillation modes is usually done by visual inspection which is time-consuming and has a degree of subjectivity. Here, we present a peak detection algorithm specially suited for the detection of solar-like oscillations. It reliably characterises the solar-like oscillations in a power density spectrum and estimates their parameters without human intervention. Furthermore, we provide a metric to characterise the false positive and false negative rates to provide further information about the reliability of a detected oscillation mode or the significance of a lack of detected oscillation modes. The algorithm presented here opens the possibility for detailed and automated peak bagging of the thousands of solar-like oscillators observed by *Kepler*.

Key words: asteroseismology – methods: data analysis – Sun: helioseismology – stars: oscillations

1 INTRODUCTION

With the advent of space observatories CoRoT (Baglin et al. 2006) and *Kepler* (Borucki et al. 2010) there are high-quality, near-uninterrupted and long (> 100 days) photometric time series measurements for an unprecedented number of stars available. For solar-like oscillators the power density spectrum (PDS) of time series data contains rich information that allows for a precise determination of fundamental stellar properties provided that individual oscillation mode parameters are measured accurately (Christensen-Dalsgaard 2004). However, most of the currently existing methods to analyse in detail the PDS require substantial human intervention. For this reason the scientific potential of the large amount of available data has not been fully exploited. Furthermore, since current methods rely on human input they carry a considerable degree of subjectivity. Therefore, a method to reliably extract all the relevant information from the measured PDS in an automated way is greatly needed. This issue will be fundamental to take advantage of upcoming missions such as TESS (Ricker et al. 2014) and PLATO (Rauer et al. 2014). It is expected that TESS and PLATO

will detect approximately 3×10^5 and 2×10^5 stars with solar-like oscillations (Huber 2018), respectively. This will greatly increase the amount of available data.

The power density spectra of solar-like oscillators have a complex structure stemming from a combination of the granulation background and the stochastically excited global oscillation modes. This makes it challenging to model the PDS accurately. The functional form of the granulation background component has been the topic of several studies (e.g. Harvey 1985; Michel et al. 2009; Kallinger et al. 2014) and it takes the form of a superposition of super-Lorentzian profiles to take into account granulation at different time scales. Additionally, each individual global stochastic oscillation mode in the power excess is well described by a Lorentzian profile, in case the mode width is larger than the frequency resolution (Kumar et al. 1988), or by a sinc^2 function otherwise (Christensen-Dalsgaard 2004). One of the main challenges in modelling the stochastic oscillations resides in identifying how many oscillation modes are visible in a given PDS realisation. Furthermore, in practice, it is desirable to have at least a crude estimate of all the parameters describing each oscillation mode. For example in a Maximum Likelihood Estimation (MLE) having a set of adequate initial values for all parameters is necessary to avoid local minima

* E-mail: ags3006@gmail.com

(Toutain & Appourchaux 1994). The Bayesian estimations using the Markov-Chain Monte-Carlo methods require an adequate prior probability distribution for each parameter which can be constructed from the initial estimates (Handberg & Campante 2011). These initial estimates can be obtained by visual inspection of the PDS since the oscillation modes produce peaks with recognisable patterns in the PDS. However, this method is not scalable to the large number of stars observed by space missions. Additionally, a visual inspection inevitably introduces a degree of subjectivity tied to the person doing the analysis. This subjectivity can partially be mitigated by assessing the statistical significance of each oscillation mode found in the PDS which prevents the inclusion of non-significant peaks in the PDS model. However, there might still be significant peaks that escape the visual inspection and are never tested for inclusion. Therefore, a reliable peak-detection method that is free from significant human input would greatly benefit the analysis of large samples of stars.

A number of peak detection algorithms have been developed over the last decades. A common approach is to search for local maxima with a signal-to-noise ratio (SNR) above a certain threshold with the SNR depending only on the peak height (e.g. Appourchaux et al. 2012). A major problem in this approach is that noise can have larger heights than some peaks caused by oscillations, this could produce a large number of either false positives or false negatives depending on the chosen SNR threshold. Furthermore, tests on the peak height would miss significant peaks that are wide but have a small height. Since most peaks in the PDS of solar-like oscillators have a width larger than the frequency resolution, this issue can be partially mitigated by smoothing before attempting a peak detection. However this approach is very sensitive to the width of the mode (i.e. its lifetime) and the amount of smoothing applied; peaks with different widths are more prominent with different amounts of smoothing. So with this approach it is impossible to choose a unique best strategy to correctly identify all features of interest.

In the current work we present a different approach based on an extension of the peak-detection algorithm proposed by Du et al. (2006) in the context of mass spectrometry. This algorithm uses a continuous wavelet transform (CWT)-based pattern-matching algorithm where there is no need for smoothing and most features are correctly identified while keeping the false positive rate low (Cruz-Marcelo et al. 2008). The CWT serves as a pattern-matching function where the signal is compared to a wavelet function specifically chosen to have similar features as the most common peaks that contain signal. The CWT has two parameters, location and scale, that regulate the position on which the matching is being calculated and the width of the feature being matched, respectively. The CWT has a similar effect as a smoothing where the amount of smoothing is variable and controlled by the scale parameter. This approach is similar to searching for narrow features with little smoothing and wide features with a larger amount of smoothing simultaneously.

Solar-like oscillators produce peaks in their PDS that are similar to the peaks studied by Du et al. (2006) which makes the CWT-based pattern-matching algorithm adequate for this context. We find that the original formulation of the algorithm is reliable when the peaks are well

separated, however it fails to correctly identify them when the modes have significant overlap, which is a common scenario in the PDS of solar-like oscillators. Furthermore, the original algorithm by Du et al. (2006) only estimates the location of the peak and not its height and width. We propose an extension which is more tolerant to peak overlap and also estimates the height and width of the peaks. To achieve these improvements we incorporate the additional assumption that the individual peaks are described by Lorentzian functions, as is the case for solar-like oscillations (Anderson et al. 1990). Additionally, we require that the PDS contains only information from the stochastically excited oscillation modes, i.e. that the PDS has been normalised to remove the granulation contributions.

In Section 2 we describe the algorithm by Du et al. (2006) and the adaptations we made for the case of analysing the PDS of solar-like oscillators. We then characterise the performance of the proposed algorithm by looking at the number false positive (Section 3) and false negative (Section 4) peak detections. In Section 5 we compare our estimation with previous studies of helioseismic data from the Birmingham Solar-Oscillations Network (BiSON) (Davies et al. 2014; Hale et al. 2016) and in Section 6 we compare our results as obtained from photometric measurements made by the *Kepler* space observatory with the results from Corsaro et al. (2015) for 19 red-giants. In each case we find similar values for the number of peaks present in the background-normalised PDS as well as their location, height and width albeit with some minor discrepancies. In contrast to previous approaches, the procedure presented here requires no human intervention which makes it more objective and suitable for the analysis of present and upcoming large data sets.¹

To study the internal structure of solar-like oscillators, the frequency of the oscillations are not sufficient. We also need to characterise each mode by its spherical degree and azimuthal order. An automated procedure to obtain this mode identification will be presented in a forthcoming paper.

2 PEAK DETECTION METHOD

The peak detection method proposed by Du et al. (2006) is based on using the continuous wavelet transform (CWT) of a signal as a pattern-matching function. The CWT of a function $s(x)$, denoted as $\mathcal{W}_\psi[s]$, is an integral transform that depends on two parameters, (a, b) , usually referred to as scale and location, respectively. It is defined as

$$\mathcal{W}_\psi[s](a, b) = \frac{1}{\sqrt{a}} \int_{-\infty}^{\infty} s(x') \overline{\psi} \left(\frac{x' - b}{a} \right) dx', \quad (1)$$

where $\psi(x)$ is a continuous function called the mother wavelet and the overline denotes complex conjugation. Intuitively, the CWT value reflects the pattern matching between the signal $s(x')$ and $\overline{\psi} \left(\frac{x' - b}{a} \right)$ with larger values representing a better match. The mother wavelet is intentionally chosen to have properties useful for a specific analysis. An appropriate mother wavelet for peak detection is the

¹ The source code implementing the algorithm presented here will be publicly available in the future as part of an automated peak-bagging pipeline.

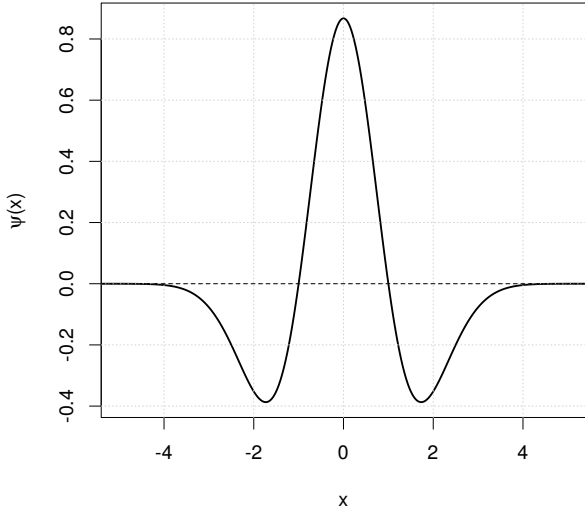


Figure 1. Mexican-hat mother wavelet as defined by (2) with $\sigma = 1$.

mexican-hat wavelet, also known as Ricker wavelet (Ricker 1944), given by

$$\psi(x) = \frac{2}{\sqrt{3}\sigma\pi^{1/4}} \left(1 - \frac{x^2}{\sigma^2}\right) e^{-x^2/2\sigma^2}. \quad (2)$$

It is the second derivative of a Gaussian function with variance σ^2 and a normalization factor such that $\int_{-\infty}^{\infty} |\psi(x')|^2 dx' = 1$ (see Fig. 1). It was shown by Du et al. (2006) that this wavelet is useful for peak finding in spectra since it has the basic features of the most common peaks in a spectrum: approximate symmetry, a major positive peak and finite width.

2.1 Single peak

We describe the peak detection method by Du et al. (2006) by illustrating it on a PDS realisation originating from a single stochastically-excited global oscillation mode. We assume that there is no contribution to the PDS other than the oscillation mode, i.e. we have a background-normalised PDS. The limit PDS in this case can be described by a Lorentzian profile. As an example we consider a Lorentzian profile with a central frequency ν_k , a height of $I_k = 10$ and a half-width at half-maximum of $\gamma_k = 0.5$, all parameters are given in arbitrary units. The frequency resolution is taken as $\delta\nu = 0.01$ also in arbitrary units. We construct a possible PDS realisation by multiplying each frequency bin by a random number drawn from an exponentially decaying probability distribution (see top panel of Fig. 2). This corresponds to a scaled χ^2 distribution with two degrees of freedom which is the probability density function of noise in a PDS. This example PDS is similar to the PDS of a single stochastically excited and damped oscillation mode. We then compute the CWT of the PDS using a mexican-hat wavelet as the mother wavelet with scale values ranging from $\delta\nu$ to the frequency range of the PDS (see middle panel of Fig. 2). Finally we look at

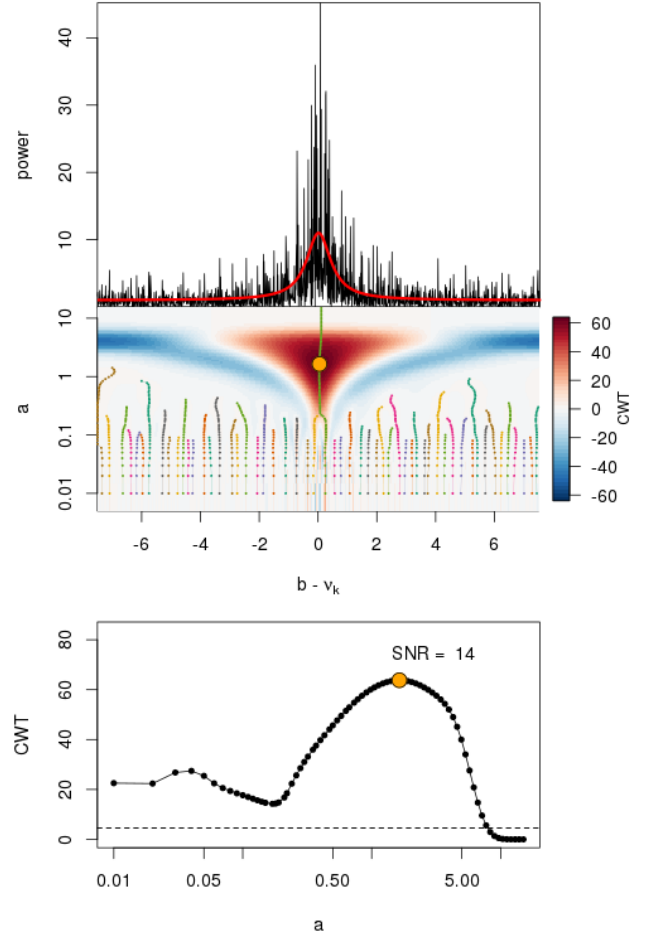


Figure 2. *Top panel:* Simulated PDS (black) realisation for a limit PDS (red) described by a Lorentzian profile with a half width at half maximum $\gamma_k = 0.5$ and height $I_k = 10$ (arbitrary units). *Middle panel:* Mexican-hat CWT of the simulated PDS realisation in the top panel as a colour map with values indicated in the side bar. The small dots are at the local maxima across each scale (a) with nearby points of the same colour being identified as belonging to the same ridge. The larger orange dot indicated the maximum CWT value for the longest ridge. *Bottom panel:* CWT as a function of scale (a) for points in the longest ridge from the middle panel. The horizontal dashed line is placed at a SNR of 1 as defined by Du et al. (2006). The orange dot is the maximum of the ridge which has a SNR close to 14.

all the local maxima in the CWT values as a function of location (b) for each scale (a). At small scales the CWT is sensitive to narrow features, which can be seen by the large number of local maxima at small values of a . Towards larger scales the CWT map becomes smoother and more sensitive to wider features.

Du et al. (2006) noted that the local maxima can be connected in ridges. The ridges produced by noise are short and have low absolute CWT values while peaks with a resolved width produce longer ridges with larger CWT values. Thus, peaks are identified by looking at ridges longer than a certain threshold which have a maximum CWT value larger than a chosen signal-to-noise ratio (SNR). To take into account the possibility of a different baseline in each peak, Du et al. (2006) proposed a SNR definition that is local for

each ridge. It is defined as the maximum CWT value on the ridge divided by the 95 percentile of the absolute value of all the CWT values at the smallest scale in a frequency range close to the ridge location. The optimal frequency range for this local noise definition depends on the problem. Here we used the implementation by [Constantine & Percival \(2016\)](#) in which the range for the local noise is ten times the frequency resolution (see bottom panel of Fig. 2).

As already mentioned, the algorithm by [Du et al. \(2006\)](#) was proposed in the context of mass spectrometry with no assumption of a particular peak shape other than being positive, approximately symmetric and with a finite width. For the particular case of finding peaks in the background-normalised PDS of solar-like oscillators we can assume that resolved oscillation modes can be modelled by Lorentzian profiles. With this assumption we can find an approximate relationship between the three parameters of the limit PDS Lorentzian (ν_k, I_k, γ_k) and the value of the CWT maximum \mathcal{W}_{\max} , its scale a_{\max} and location b_{\max} . By making 5000 simulations of this single-peak scenario with representative values, in arbitrary units, of $I_k \in (10, 200)$ and $\gamma_k \in (5, 30)$ we derived the following empirical relationships:

$$\nu_k \simeq b_{\max} \quad (3)$$

$$\gamma_k \simeq 1.26 + 0.32 a_{\max} \quad (4)$$

$$I_k \simeq 2.30 \left(\mathcal{W}_{\max} \sqrt{\delta\nu/a_{\max}} \right)^{0.93}, \quad (5)$$

where $\delta\nu$ is the PDS frequency resolution simulated to be in the range $\delta\nu \in (0.01, 1)$. Equations (3)–(5) are not relevant for the algorithm as formulated by [Du et al. \(2006\)](#), we will however use them later as a first characterisation of the oscillation modes in solar-like oscillators.

2.2 Multiple peaks

Unlike the example in Fig. 2 with one mode, solar-like oscillators show several oscillation modes in their PDS. The limit PDS is thus a superposition of several Lorentzian profiles. The peak detection method by [Du et al. \(2006\)](#) is adequate when the overlap between these Lorentzian profiles is small, however it is less reliable when the overlap is significant. When the separation between two peaks is large there are two ridges in the CWT each one with a large SNR (see left panel of Fig. 3). As the central frequencies get closer the SNR of the ridge corresponding to the peak with smaller amplitude decreases considerably until it has a SNR similar to the noise even though it is visible by eye in the PDS realisation (see right panel of Fig. 3). Reducing the SNR threshold for such cases usually produces several false positive identifications.

To overcome this limitation we now propose an adjustment to the peak-detection algorithm by [Du et al. \(2006\)](#) for the context of solar-like oscillators. We use the same CWT with the mexican-hat mother wavelet and use the same approach to find the ridges of local CWT maxima. We modify the SNR definition using our knowledge about the statistical distribution of noise in a PDS realisation. In this modified SNR definition we consider a global instead of a local noise level since a background-normalised PDS has a constant baseline. We simulated a PDS realisation of pure white noise, which has a constant limit PDS with value 1, and defined as noise the 95 percentile of the absolute values of all

the CWT coefficients at the lowest scale, which we choose as the frequency resolution $\delta\nu$. With this SNR definition the noise has a value of approximately 2 and thus the SNR is defined as half the maximum CWT value in a ridge. This definition is adopted throughout this work.

Furthermore, in contrast to the approach taken by [Du et al. \(2006\)](#) which considers only the global maximum on each ridge, we consider all local maxima since their occurrence frequently indicate a significant peak overlap. By using Eqs. (3)–(5) each one of these local maxima represents a possible Lorentzian profile in the limit PDS (see Fig. 4). Thus, each combination of local maxima in the CWT ridges is considered as a possible PDS model. However, when there are multiple peaks partially overlapping the CWT values close to the location of a peak are reduced by a negative contribution from neighbouring peaks. This usually results in a displacement of some local maxima in a ridge to lower scales and, subsequently, an underestimation of γ_k for some peaks when using Eqs. (3)–(5). We correct for this underestimation by an MLE parameter optimisation using the values obtained from Eqs. (3)–(5) as initial estimates (see Fig. 5). Finally, to select the most appropriate model for the PDS from all the possible combinations we use the Akaike Information Criterion (AIC) which penalises the likelihood of the model with its complexity to avoid over-fitting ([Akaike 1998](#)). Since a lower AIC value is indicative of a better model, we select the most appropriate model as the one with the lowest AIC.

Since the total number of local maxima in all the ridges is usually of the order $10^2 - 10^3$, depending on the chosen SNR threshold, comparing all combinations of these points as possible PDS models is computationally expensive. We reduce the computational time by considering different segments of the PDS separately. In the first step we select the local CWT maxima that has the highest scale. According to Eqs. (3)–(5) this corresponds to a peak located at a certain frequency ν_k and a line width γ_k . We define a PDS region local to this peak as the PDS in the frequency range $\nu_k \pm 2\gamma_k$. Finally, we consider all the local maxima in this region and select the best model as described before.

The algorithm presented here works optimally for oscillations that have a width larger than the frequency resolution of the PDS. This might not be the case for some of the oscillations. In such circumstances the peak is best modelled by a sinc^2 profile. We find these oscillations by performing the peak detection as described above and looking at the residuals of this fit with a false-alarm probability test for a single frequency bin ([Appourchaux et al. 2012](#)).

3 FALSE POSITIVE PEAK DETECTIONS

Since noise in the PDS can generate false positive detections, it is useful to assess the probability that a given peak can be generated only by random chance. A significance test can be made by the ratio between the likelihood of the observed PDS assuming a model with the peak included and its likelihood if the peak is omitted from the model. Alternatively, the AIC difference between both models provides a similar and more robust test that penalises for the number of degrees of freedom in the model. Complementary to these tests, the wavelet-based SNR described previously can also be used as a significance test that is sensitive to different features of

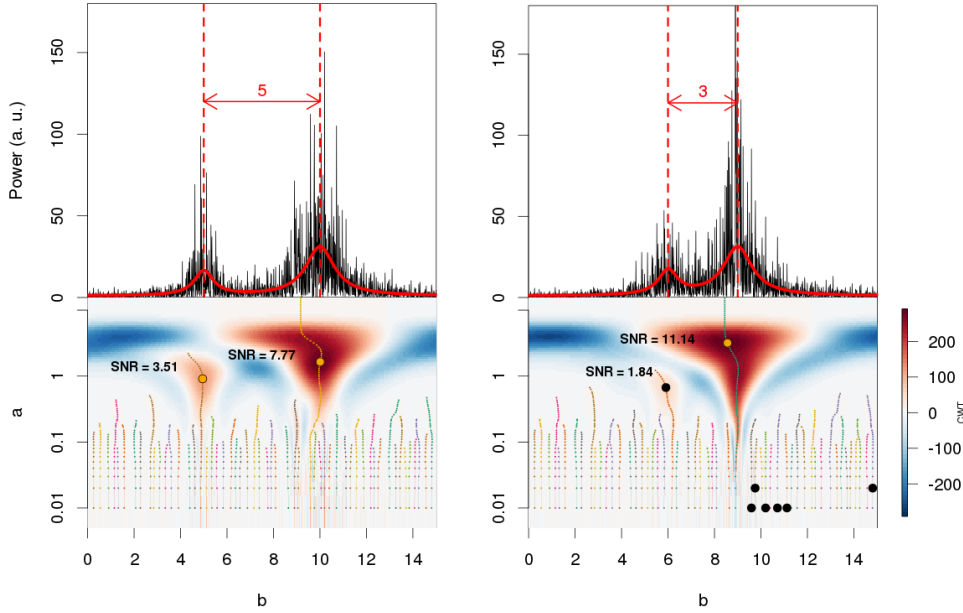


Figure 3. *Left panels:* The upper part shows a limit PDS represented by two Lorentzian profiles with heights $I_1 = 120$ and $I_2 = 150$, half widths at half maximum $\gamma_1 = 0.5$, $\gamma_2 = 0.75$ and central frequencies $\nu_2 - \nu_1 = 5$ (red) and the simulated PDS realisation (black). The bottom part shows a colour map of the CWT of the simulated PDS realisations with the identified ridges as small dots. The bigger orange dots are at the maximum CWT values on each ridge that have a SNR greater than 3 as defined by [Du et al. \(2006\)](#). *Right panels:* Same as before with a reduced distance between the central frequencies to $\nu_2 - \nu_1 = 3$. The black dots are at the maximum CWT value for ridges with SNR greater or equal than 1.84 and smaller than 3.

the PDS. Since our algorithm uses a mexican-hat mother wavelet, which has the general shape of the most common peaks, the SNR is particularly suited to assess the significance of solar-like oscillations. The wavelet-based SNR is, on average, a monotonically increasing function of the AIC difference between a PDS model with the peak and without it. However, their relationship is non linear and has considerable spread so they provide to some extent complementary information. In this section we describe the statistical properties of the SNR for peaks generated purely by random noise in the PDS and quantify the number of such peaks that we can expect to detect in any given PDS realisation.

To estimate the chance of false positive peak detections we generated 10^5 PDS each one containing 10^4 frequency bins with only noise having the same distribution as the noise in a background-normalised PDS, i.e. a scaled χ^2 distribution with 2 degrees of freedom. We applied the wavelet-based peak detection method described here to all the generated PDS and aggregated the results. We found that there is a 10^{-3} chance per frequency bin in a PDS of having a false positive detection with a SNR greater than 1.1 and an AIC difference greater than 0. For a typical *Kepler* PDS this amounts to approximately 30 false positives in the whole PDS. However, the number is reduced when considering only the power excess region (see below).

The false-positive detections have different amplitudes and their number depends on the SNR threshold. To quantitatively characterise this dependence we define $N_{\text{fp}}(A, s)$ to be the number of false-positive peak detections that have an amplitude greater than or equal to A and a SNR greater than or equal to s . Since the number $N_{\text{fp}}(A, s)$ depends also on the number of frequency bins, n , in the PDS it is more

convenient to normalise it by n (see Fig. 6 N_{fp}/n). Additionally, to take into account the PDS frequency resolution, $\delta\nu$, we calculate N_{fp} as a function of $A' = A/\sqrt{\delta\nu}$. By using symbolic regression ([Searson 2015](#)) we discovered that N_{fp} can be described by a function that is symmetric in A' and s and has the form

$$\begin{aligned} \log(N_{\text{fp}}) = & c_0 + c_1 s + c_2 A' \\ & + c_3 s^2 + c_4 A'^2 + c_5 s A' \\ & + c_6 (s A')^2 + c_7 (A'/s)^2 + c_8 (s/A')^2 + \log(n). \end{aligned} \quad (6)$$

We further refined the symbolic regression estimate of the coefficients c_i by using a multiple linear regression with the same model. That is, we considered $\{s, A', s^2, A'^2, s A', (s A')^2, (A'/s)^2, (s/A')^2\}$ as linear predictors for $\log(N_{\text{fp}}/n)$ and performed a least squares regression to estimate c_i . The obtained coefficient values, their standard error and the null hypothesis probability for each term (p -value) are reported in Table 1.

To calculate N_{fp} we must also provide the number of frequency bins n under consideration. The value of N_{fp} will change considerably whether we take n as the number of frequency bins in the whole PDS or only in the power excess region. Since we only expect stochastically excited global oscillations in the power excess region we adopt n as the number of frequency bins in the power excess region. To define this region precisely we adopt the global description of the power excess as a gaussian function centred at ν_{max} with a width of the gaussian σ_{env} and take n as the number of frequency bins in $\nu_{\text{max}} \pm 4\sigma_{\text{env}}$. This definition is adopted throughout this work.

In summary, given a peak amplitude A and SNR s we

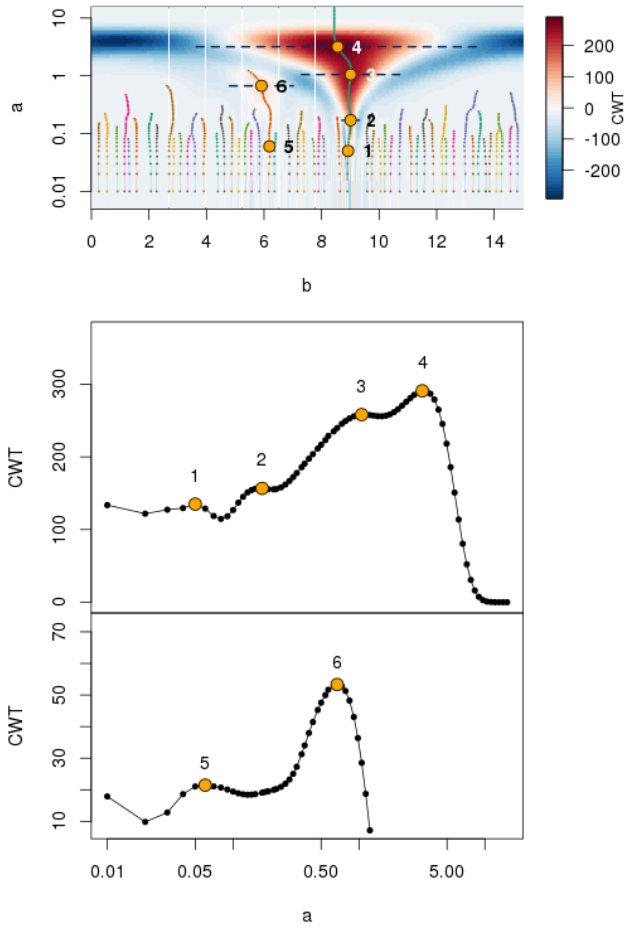


Figure 4. *Top panel:* CWT of the simulated PDS realisation from the right panel of Fig. 3 as a colour map with the identified ridges as small dots. The larger orange dots are at the local CWT maxima of the two longest ridges. The horizontal dashed lines span $4\gamma_k$ for each point as inferred from Eq. (4). *Middle and bottom panels:* CWT as a function of scale (a) for the longest and second longest ridges in the CWT map from the top panel, respectively. The orange points denote the local maxima with the labels being the same as in the top panel.

Table 1. Least-squares linear regression estimate for the parameter values, standard errors and null-hypothesis probability (p -value) for each parameter in Eq. 6.

	estimate	standard error	p -value
c_0	-9.63	1.18	2.67×10^{-14}
c_1	3.99	0.75	2.13×10^{-7}
c_2	2.24	0.36	1.88×10^{-9}
c_3	-0.21	0.06	1.94×10^{-4}
c_4	-0.07	0.01	1.49×10^{-6}
c_5	-1.93	0.19	7.99×10^{-20}
c_6	0.027	0.003	1.73×10^{-15}
c_7	-0.14	0.01	4.30×10^{-32}
c_8	-2.78	0.24	1.71×10^{-25}

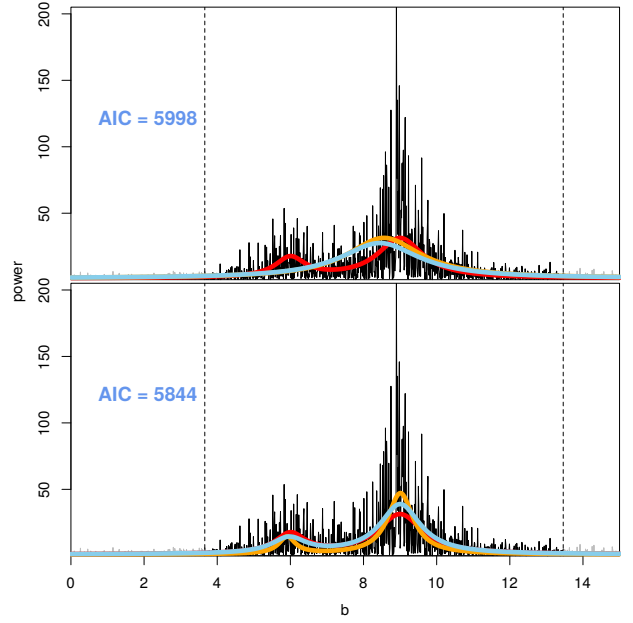


Figure 5. Same simulated PDS realisation (black) and limit PDS (red) as the right panel of Fig. 3. The vertical dashed lines are at $\nu_k \pm 2\gamma_k$ as obtained from Eqs. (3)–(5) for point 4 from Fig. 4. In orange a PDS model is shown based on Eqs. (3)–(5) using point 4 (*top panel*) and points 3 and 6 (*bottom panel*). In blue is the model obtained after an MLE parameter optimisation using the previous values as initial guesses in the range $\nu_k \pm 2\gamma_k$. The AIC values of the MLE are calculated in the PDS region delimited by the vertical dashed lines. A lower AIC indicates a better model.

can estimate N_{fp} using Eq. (6) using $A' = A/\sqrt{\delta\nu}$. The number N_{fp} is the expected number of false positives in the power excess region that have an amplitude equal or greater than A and a SNR equal or greater than s . A value of N_{fp} greater than 1 indicates that the peak is more likely to have been generated by noise than from a real signal. Conversely, if N_{fp} is smaller than 1, it is more probable that the peak originates from a process different than noise. Smaller values of N_{fp} denote that a peak is less likely to be a false positive detection.

4 DETECTION PROBABILITY

Complementary to assessing the significance of a peak detection, we now address the significance of the lack of detections, that is, for a given peak amplitude we estimate the probability that the algorithm presented here can recognise it among the noise. To estimate this detection probability we simulated 10^5 different PDS each one with a Lorentzian peak multiplied by noise as described in section 2.1. The Lorentzian peaks were generated with parameters in the ranges $\gamma_k/\delta\nu \in (2, 10)$ and $I \in (1, 10)$ in arbitrary units. We then applied the algorithm presented here to the PDS using a SNR of 1.1 and attempted to recover the input peak. From these simulations we estimated the proportion of times P that a peak with linewidth $\gamma_k/\delta\nu$ was not successfully recovered (see Fig. 7). It can be seen from Fig. 7 that P can be described as a function of $\gamma_k/\delta\nu$ alone. In this case it is not necessary to use a model discovery technique, like symbolic

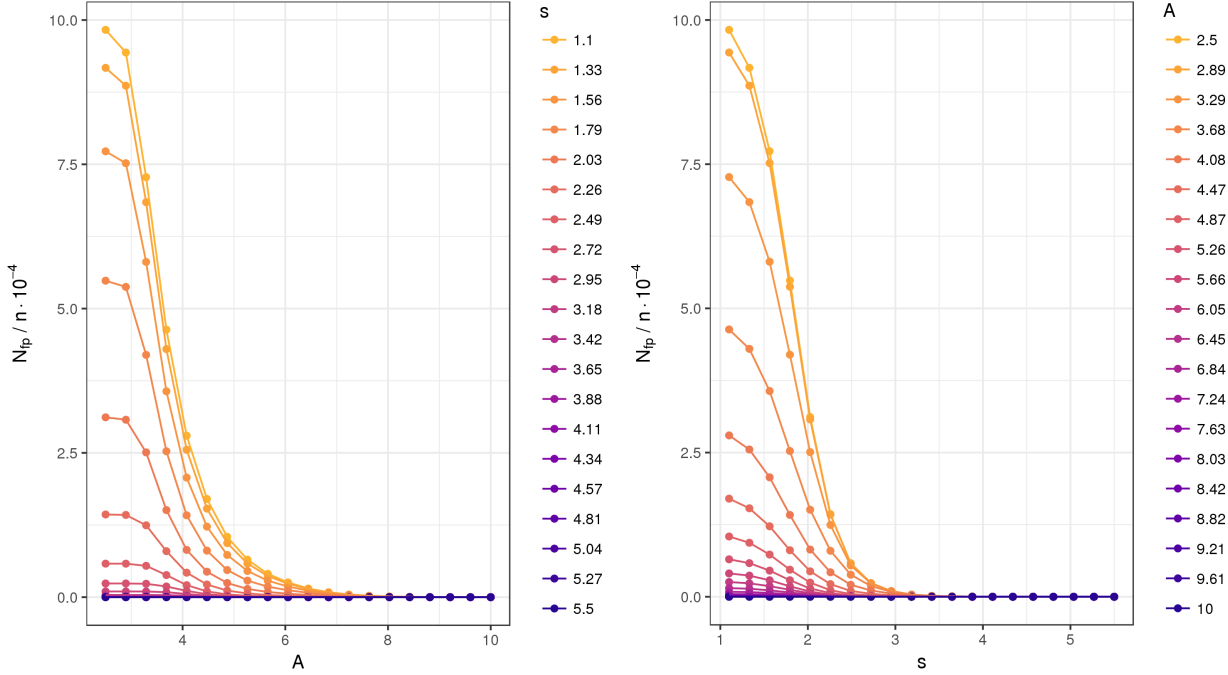


Figure 6. Expected number of false-positive detections N_{fp} per number of frequency bins n of peaks having a SNR greater than or equal to s and an amplitude greater than or equal to A . The *left panel* shows A as the independent variable with s as a colour code while in the *right panel* the roles are inverted to show the symmetry between A and s .

Table 2. Same as Table 1 for Eq. 7.

	estimate	standard error	p -value
d_0	0.09	$< 10^{-4}$	3.11×10^{-130}
d_1	-0.49	$< 10^{-4}$	1.34×10^{-107}
d_2	0.18	$< 10^{-4}$	5.94×10^{-67}
d_3	-0.06	$< 10^{-4}$	6.71×10^{-26}

regression. Instead we propose a polynomial model in the form.

$$P = \sum_{i=0}^N d_i \left(\frac{\gamma_k}{\delta\nu} \right)^i \quad (7)$$

for some coefficients d_i with N being the degree of the polynomial. We estimated the coefficients d_i by a multiple linear regression, similar to Sec. 3, for increasing values of N and found that the model with the lowest AIC is a third degree polynomial ($N = 3$). We adopt this model throughout this work and give in Table 2 the estimated coefficients d_i , their standard error and null hypothesis probability for each term (p -value).

In summary, for a predicted peak with linewidth γ_k and a PDS frequency resolution $\delta\nu$ we can calculate the probability that the algorithm will not find the peak, P , using Eq. 7.

5 SOLAR FREQUENCIES OBSERVED BY BISON

As a proof of concept for the peak detection algorithm presented here we analyse the solar stochastically excited global

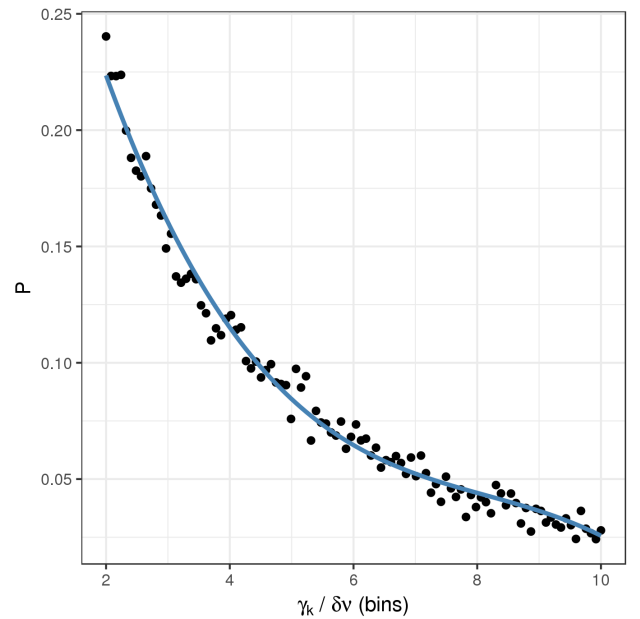


Figure 7. Probability (P) of not finding a peak of a given linewidth γ_k where $\delta\nu$ is the PDS frequency resolution. The blue line is the fit using Eq. 7.

oscillations modes obtained from radial velocity variations measured by the Birmingham Solar Observatory Network (BiSON). We used the time series from the 1st January 1991 to the 31st December 2015 optimised for fill (Davies et al. 2014; Hale et al. 2016). We calculated the PDS from the discrete Fourier transform of the time-series normalised us-

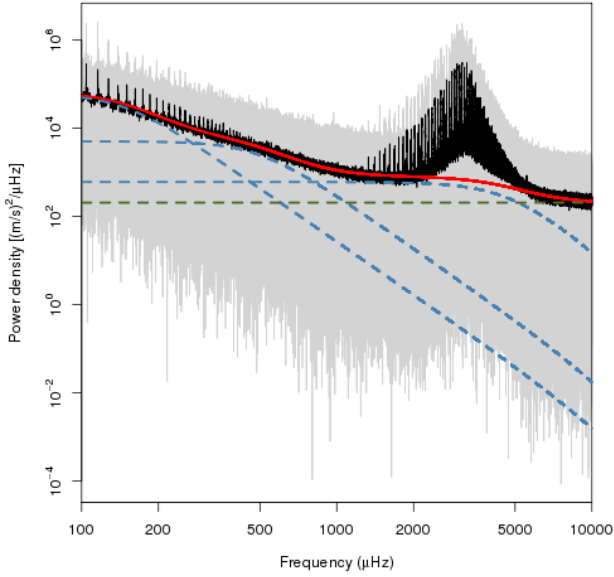


Figure 8. PDS (grey) of the radial velocity measurements by BiSON with a $0.1\mu\text{Hz}$ binned version (black). The background function is shown in red with the individual granulation components in blue and the white noise in green.

ing the spectral window function (Kallinger et al. 2014) (see Fig. 8).

For the CWT-based peak detection algorithm we need to normalise the PDS by an estimation of the granulation background. As an estimation of this background we used a superposition of three granulation components in the form of super-Lorentzians $A_i/[1 + (\nu/b_i)^4]$ and a white noise P'_n . The oscillation power excess region in this dataset is difficult to model accurately so we excluded it from our fit. Specifically, during the parameter estimations we computed the likelihood of the PDS model only for the region outside the frequency interval ranging from 1200 to 5000 μHz . Thus we fitted a PDS model containing only the granulation background in the form

$$P(\nu) = P'_n + \eta(\nu)^2 \left[\sum_{i=1}^3 \frac{A_i}{1 + (\nu/b_i)^4} \right], \quad (8)$$

where $\eta(\nu) = \text{sinc}(\pi\nu/2\nu_{\text{ny}})$ is a frequency-dependent damping, consequence of the measurement discretisation process, (Chaplin et al. 2011) and ν_{ny} is the Nyquist frequency.

To estimate the model parameters we used the affine invariant Markov-chain Monte-Carlo algorithm by Goodman & Weare (2010), as implemented by Foreman-Mackey et al. (2013). We estimated the posterior probability density function (PDF) for each parameter using the chains after convergence was reached. The expectation value for each parameter was estimated as the median of its PDF. Additionally, we estimated the uncertainties by the 16-84 percentiles of each PDF. The obtained parameter estimations with their

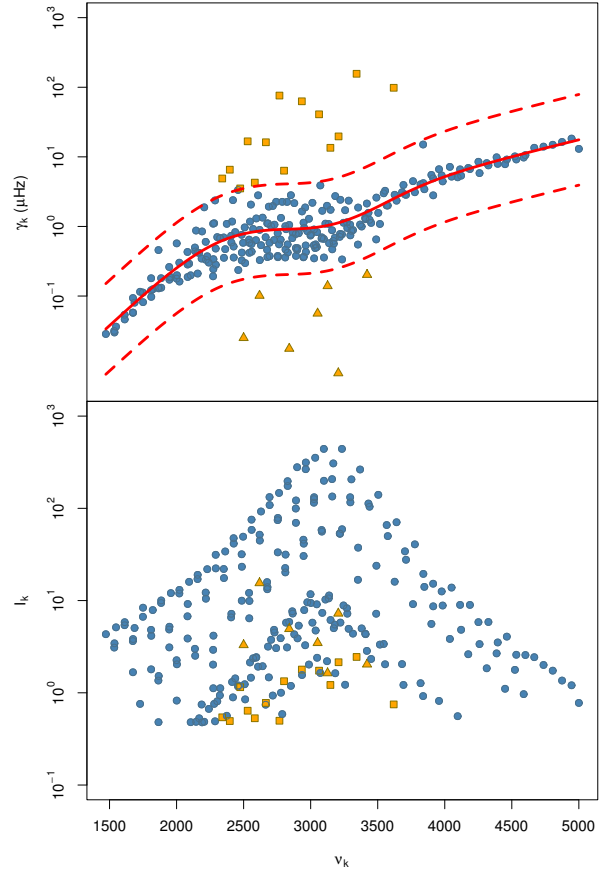


Figure 9. Half-width at half maxima (γ_k , top) and heights (I_k bottom) as functions of frequency for the peaks identified in the PDS of the solar radial velocity measurements by BiSON. The solid red line in the top panel is a smoothing cubic spline to the data; the dashed red lines are the spline multiplied by $e^{\pm 1.5}$. The points outside the region delimited by the dashed lines are coloured orange. The square symbols for the outliers denote peaks with a larger width while the triangular symbols denote a smaller width.

uncertainties are:

$$\begin{aligned} P_n &= 2.06^{+0.02}_{-0.02} \times 10^2 (m/s)^2 / \mu\text{Hz}, \\ A_1 &= 6.09^{+0.77}_{-0.60} \times 10^4 (m/s)^2 / \mu\text{Hz}, \\ b_1 &= 1.45^{+0.08}_{-0.08} \times 10^2 \mu\text{Hz}, \\ A_2 &= 5.04^{+0.61}_{-0.59} \times 10^3 (m/s)^2 / \mu\text{Hz}, \\ b_2 &= 4.95^{+0.26}_{-0.22} \times 10^2 \mu\text{Hz}, \\ A_3 &= 6.06^{+0.35}_{-0.38} \times 10^2 (m/s)^2 / \mu\text{Hz}, \\ b_3 &= 4.60^{+0.12}_{-0.10} \times 10^3 \mu\text{Hz}. \end{aligned}$$

Even though this granulation background description is too simplistic to accurately describe all phenomena contributing to the BiSON PDS, it is sufficiently accurate for our purpose of finding the most relevant signatures of the stochastically excited global oscillations (see Fig. 8).

Having obtained a background-normalised PDS we proceeded to apply our peak detection algorithm to it. However,

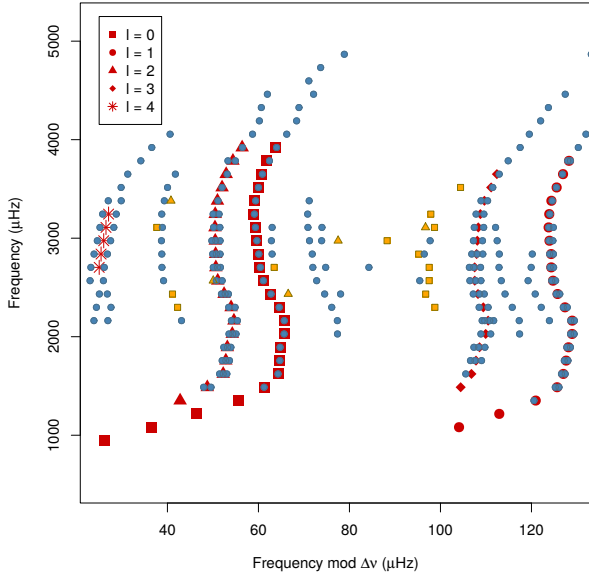


Figure 10. Échelle diagram of the peaks shown in Fig. 9 with the same colouring and symbol scheme. In red are a combination of the oscillations found by Chaplin et al. (1996); Broomhall et al. (2009) and Davies et al. (2014); the symbol identifies the spherical harmonic degree l according to the legend.

due to the large size of the BiSON data set, it was not computationally feasible to use the peak detection algorithm on the full PDS. Instead, we analysed segments of the PDS spanning $500 \mu\text{Hz}$ each in steps of $150 \mu\text{Hz}$ so that there is a $350 \mu\text{Hz}$ overlap between each consecutive segment, to avoid possible edge effects in the CWT, and combined the resulting peaks. Figure 9 shows the frequencies of the identified peaks, ν_k , as a function of γ_k (top) and l_k (bottom). The points follow the same frequency-dependant γ_k as found by Chaplin et al. (1997). The red solid line in the top panel of Fig. 9 is a smoothing cubic spline that shows the overall trend; the dashed red lines are the spline fit multiplied by $e^{\pm 1.5}$ and delimit a region where most points lie. The outliers from this trend have been coloured in orange in order to distinguish them from the rest. Most outliers from this trend have a relatively small height (see bottom panel of Fig. 9). We interpret the wide outliers as not being stochastically excited global oscillations but originating as a compensation for an incomplete description of the granulation background.

In Fig. 10 we use an échelle diagram to compare the frequency of the solar-like oscillation modes found with the peak-detection method presented here with the results obtained by Chaplin et al. (1996), Broomhall et al. (2009) and Davies et al. (2014). All oscillations with a frequency higher than $\sim 1400 \mu\text{Hz}$ are correctly identified. The lowest frequency modes are not found with the CWT-based method because their width is small and the CWT-based pattern-matching is optimal for peaks with a width that can be resolved. It is also visible that, due to rotational splitting, most oscillation modes with $l > 0$ are detected as having more than one peak. Figure 11 shows an example of a rotational split $l = 2$ mode compared with the reported values by Davies et al. (2014). It should be noted that Davies et al.

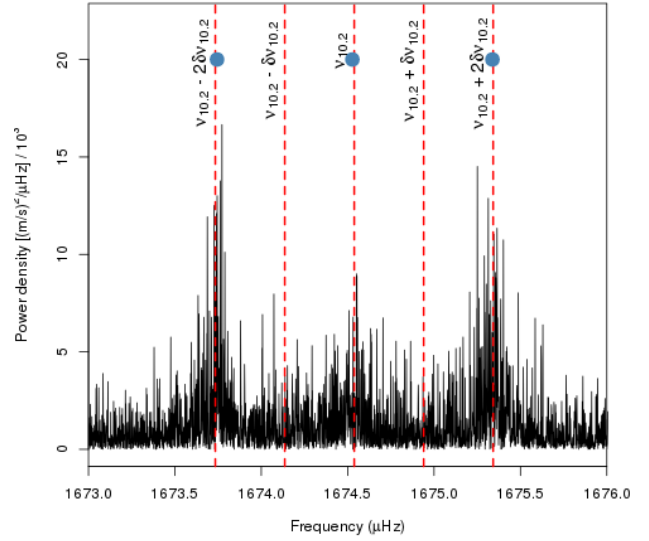


Figure 11. PDS (black) of the radial velocity measurements by BiSON. The dashed red lines are located at the frequencies $\delta\nu_{n,l} + m\delta\nu_{n,l}$ for $n = 10$ and $l = 2$ as reported by Davies et al. (2014). The blue dots are located at the frequencies of the peaks identified in this work.

(2014) fit for each spherical degree, l , a model described by the central frequency $\nu_{n,l}$ and the rotational splitting $\delta\nu_{n,l}$ whereas the method presented here finds each oscillation frequency individually.

There are also several ridges detected that are not reported in the literature as stochastically excited oscillation modes. The origin of these peaks can be traced back to the window function of BiSON observations which produces prominent aliases of the oscillation modes. We find more oscillation modes at higher frequencies than reported in the literature.

6 RED-GIANTS OBSERVED BY KEPLER

The CWT-based peak detection presented here is capable of identifying the solar-like oscillations in the red-giant stars observed by Kepler. We use the set of 19 red-giant stars studied in detail by Corsaro et al. (2015) to compare our results. The Kepler light curves used in this work have been extracted using the pixel data following the methods described in Mathur et al. (in preparation) and corrected following Garcia et al. (2011)². We calculated the PDS from the corrected time-series using a Lomb-Scargle periodogram (Scargle 1982) normalised using the spectral window function (Kallinger et al. 2014).

² This data preparation procedure includes concatenating the light curves from different quarters, correcting for the levels of each quarter, thermal drifts and jumps and removing a second order polynomial.

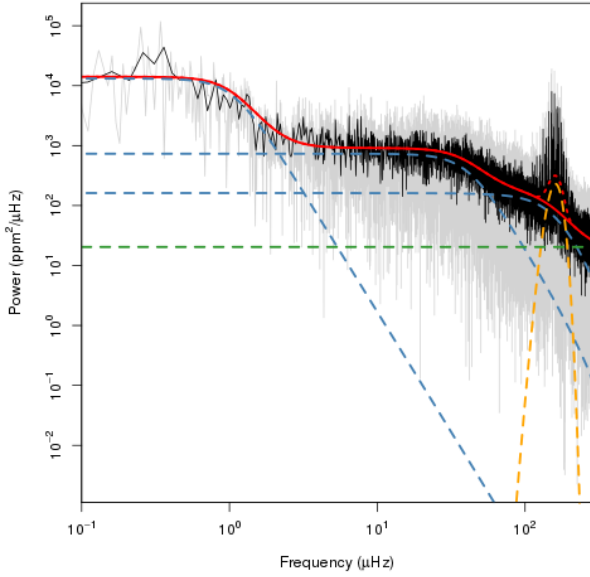


Figure 12. Background fit of KIC 12008916. The PDS is shown in gray with a binned version in black. The solid red line is the background without the power excess while the dotted red line is the background fit plus the power excess. The individual granulation components are shown in blue, the power excess in orange and the white noise in green dashed lines.

To obtain a background-normalised PDS we fit the following model

$$P(\nu) = P'_n + \eta(\nu)^2 \left[\sum_{i=1}^3 \frac{A_i}{1 + (\nu/b_i)^4} + P_g \exp\left(\frac{\nu - \nu_{\max}}{\sigma_{\text{env}}}\right)^2 \right] \quad (9)$$

to the observed PDS. To estimate the model parameters we adopt a Bayesian framework and use the MCMC algorithm of [Goodman & Weare \(2010\)](#) as implemented by [Foreman-Mackey et al. \(2013\)](#) to estimate the posterior density function of each parameter. The expectation value for each parameter is approximated as the median of its posterior density function and the standard errors are approximated as the 16-84 percentiles. An example of the resulting background fit is shown in Fig. 12 for KIC 12008916. The estimated background parameter values and their uncertainties are given in Appendix A.

We subsequently identified the resolved oscillation modes in the background-normalised PDS using the peak-detection algorithm presented here with a SNR threshold of 1.1 discarding any detections with an AIC smaller than 0 and a N_{fp} greater than 1. As discussed in section 2, the CWT is suitable to detect peaks with a width larger than the frequency resolution. However, in some red-giant stars there are gravity-dominated mixed modes visible which can have peaks narrower than the frequency resolution, i.e. they are unresolved. To highlight the unresolved oscillation modes we make a PDS model with the peaks detected with the CWT and divide the background-normalised PDS by this model. The resulting PDS (see the middle panel of Fig. 13) contains only the unresolved oscillations on top of the noise. The peaks that have a false-alarm probability lower than a

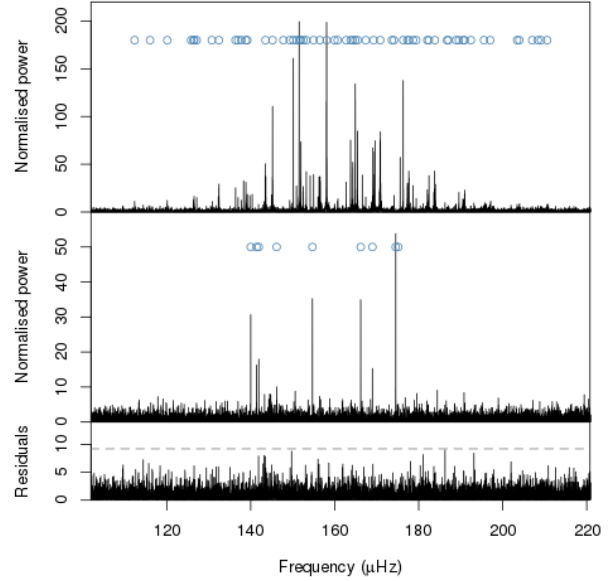


Figure 13. *Top panel:* Background-normalised PDS for KIC 12008916. The blue circles indicate the location of the oscillation modes identified with the peak detection algorithm presented here. *Middle panel:* PDS from the top panel divided by a PDS model containing the peaks identified previously. The blue circles indicate the location of points having a false-alarm probability lower than 10^{-4} . *Bottom panel:* Residual power obtained by dividing the PDS from the top panel by a model containing all the resolved and unresolved oscillations identified with their parameters optimised with a MLE on the whole background-normalised PDS. The dashed horizontal line is placed at a level corresponding to a false-alarm probability of 10^{-4} .

certain threshold, which we choose to be 10^{-4} , are deemed significant and fitted with a sinc^2 function.

To mitigate possible power leakage between the peaks in the PDS we apply a final MLE to the full background-normalised PDS taking the detections of both resolved and unresolved oscillation modes into account. This provides our final identification of the solar-like oscillations visible in the PDS.

We compared our peak identifications with the values reported by [Corsaro et al. \(2015\)](#). Both methods agree on most of the detections although there are some discrepancies specially when the peaks have low amplitude or significant overlap (see Figs. 14 and 15). The resolved and unresolved oscillation modes detected for KIC 12008916 are shown in Tables B37 and B38 respectively. We provide the parameters of the detected oscillations for the remaining stars in the sample analysed by [Corsaro et al. \(2015\)](#) in Appendix B.

7 DISCUSSION AND CONCLUSIONS

Here we have addressed the problem of finding the significant solar-like oscillations in a background normalised power density spectra (PDS). We presented a peak finding algorithm capable of finding the oscillation modes in a PDS and provide an estimate of their model parameters provided that the PDS background description is adequate. Furthermore, for

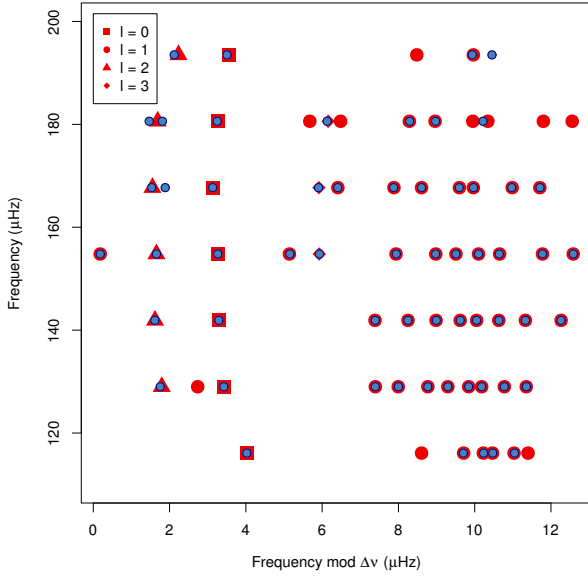


Figure 14. Échelle diagram with the frequencies of the solar-like oscillation modes of KIC 12008916 using $\Delta\nu = 12.9 \mu\text{Hz}$. Red symbols by Corsaro et al. (2015) with their shape identifying the spherical degree. The blue circles are the frequencies detected by the method presented here.

each detected mode we assess its probability of being a false positive detection. Additionally, for a predicted peak we can estimate the probability of the algorithm being able to detect it. In contrast to other approaches the algorithm is fast (less than a minute for a typical *Kepler* long-cadence PDS) and does not require human intervention making it suitable for the analysis of large samples of stars. Since the algorithm does not rely on human intervention, it provides an objective criteria for peak selection in the fitted PDS model. We have shown that the results obtained from the peak detection algorithm presented here are comparable to previous approaches. The peak detection algorithm presented here together with an adequate background description, and the spherical degree, and azimuthal order determination for each mode enables the study of the internal structure of the large number of solar-like oscillators that are already observed and yet remain unexplored.

ACKNOWLEDGEMENTS

The research leading to the presented results has received funding from the European Research Council under the European Community's Seventh Framework Programme (FP7/2007-2013)/ERC grant agreement no 338251 (StellarAges). This work partially used data analyzed under the NASA grant NNX12AE17. The authors also acknowledge the anonymous referee for the helpful and constructive comments.

REFERENCES

- Akaike H., 1998, *Information Theory and an Extension of the Maximum Likelihood Principle*. Springer New York, New York, NY, pp 199–213, [doi:10.1007/978-1-4612-1694-0_15](https://doi.org/10.1007/978-1-4612-1694-0_15)
- Anderson E. R., Duvall Jr. T. L., Jefferies S. M., 1990, *ApJ*, **364**, 699
- Appourchaux T., et al., 2012, *A&A*, **543**, A54
- Baglin A., et al., 2006, in 36th COSPAR Scientific Assembly.
- Borucki W. J., et al., 2010, *Science*, **327**, 977
- Broomhall A.-M., Chaplin W. J., Davies G. R., Elsworth Y., Fletcher S. T., Hale S. J., Miller B., New R., 2009, *Monthly Notices of the Royal Astronomical Society: Letters*, **396**, L100
- Chaplin W. J., Elsworth Y., Howe R., Isaak G. R., McLeod C. P., Miller B. A., New R., 1996, *Monthly Notices of the Royal Astronomical Society*, **280**, 1162
- Chaplin W. J., Elsworth Y., Isaak G. R., McLeod C. P., Miller B. A., New R., 1997, *Monthly Notices of the Royal Astronomical Society*, **288**, 623
- Chaplin W. J., et al., 2011, *The Astrophysical Journal*, **732**, 54
- Christensen-Dalsgaard J., 2004, *Solar Physics*, **220**, 137
- Constantine W., Percival D., 2016, *wmtsa: Wavelet Methods for Time Series Analysis*. <https://CRAN.R-project.org/package=wmtsa>
- Corsaro E., De Ridder J., García R. A., 2015, *A&A*, **579**, A83
- Cruz-Marcelo A., Guerra R., Vannucci M., Li Y., Lau C. C., Man T.-K., 2008, *Bioinformatics*, **24**, 2129
- Davies G. R., Chaplin W. J., Elsworth Y., Hale S. J., 2014, *Monthly Notices of the Royal Astronomical Society*, **441**, 3009
- Du P., Kibbe W. A., Lin S. M., 2006, *Bioinformatics*, **22**, 2059
- Foreman-Mackey D., Hogg D. W., Lang D., Goodman J., 2013, *PASP*, **125**, 306
- García R. A., et al., 2011, *Monthly Notices of the Royal Astronomical Society: Letters*, **414**, L6
- Goodman J., Weare J., 2010, *Communications in Applied Mathematics and Computational Software*, **5**, 65
- Hale S. J., Howe R., Chaplin W. J., Davies G. R., Elsworth Y. P., 2016, *Solar Physics*, **291**, 1
- Handberg R., Campante T. L., 2011, *A&A*, **527**, A56
- Harvey J., 1985, in Rolfe E., Battrick B., eds, *ESA Special Publication Vol. 235, Future Missions in Solar, Heliospheric & Space Plasma Physics*.
- Huber D., 2018, in Campante T. L., Santos N. C., Monteiro M. J. P. F. G., eds, *Asteroseismology and Exoplanets: Listening to the Stars and Searching for New Worlds: IVth Azores International Advanced School in Space Sciences*. Springer International Publishing, Cham, pp 119–135, [doi:10.1007/978-3-319-59315-9_6](https://doi.org/10.1007/978-3-319-59315-9_6)
- Kallinger T., et al., 2014, *A&A*, **570**, A41
- Kumar P., Franklin J., Goldreich P., 1988, *ApJ*, **328**, 879
- Michel E., Samadi R., Baudin F., Barban C., Appourchaux T., Auvergne M., 2009, *A&A*, **495**, 979
- Rauer H., et al., 2014, *Experimental Astronomy*, **38**, 249
- Ricker N., 1944, *Geophysics*, **9**, 314
- Ricker G. R., et al., 2014, *Proc.SPIE*, **9143**, 9143
- Scargle J. D., 1982, *ApJ*, **263**, 835
- Searson D. P., 2015, in Gandomi A. H., Alavi A. H., Ryan C., eds, *Handbook of Genetic Programming Application*. Springer International Publishing, Switzerland, Chapt. 22, pp 551–573
- Toutain T., Appourchaux T., 1994, *A&A*, **289**, 649

APPENDIX A: RESULTS FOR THE GLOBAL PDS FITS

We performed a global PDS fit for the 19 red-giant stars analysed by Corsaro et al. (2015) using Eq. (9) and the procedure described in Section 6. The obtained parameter val-

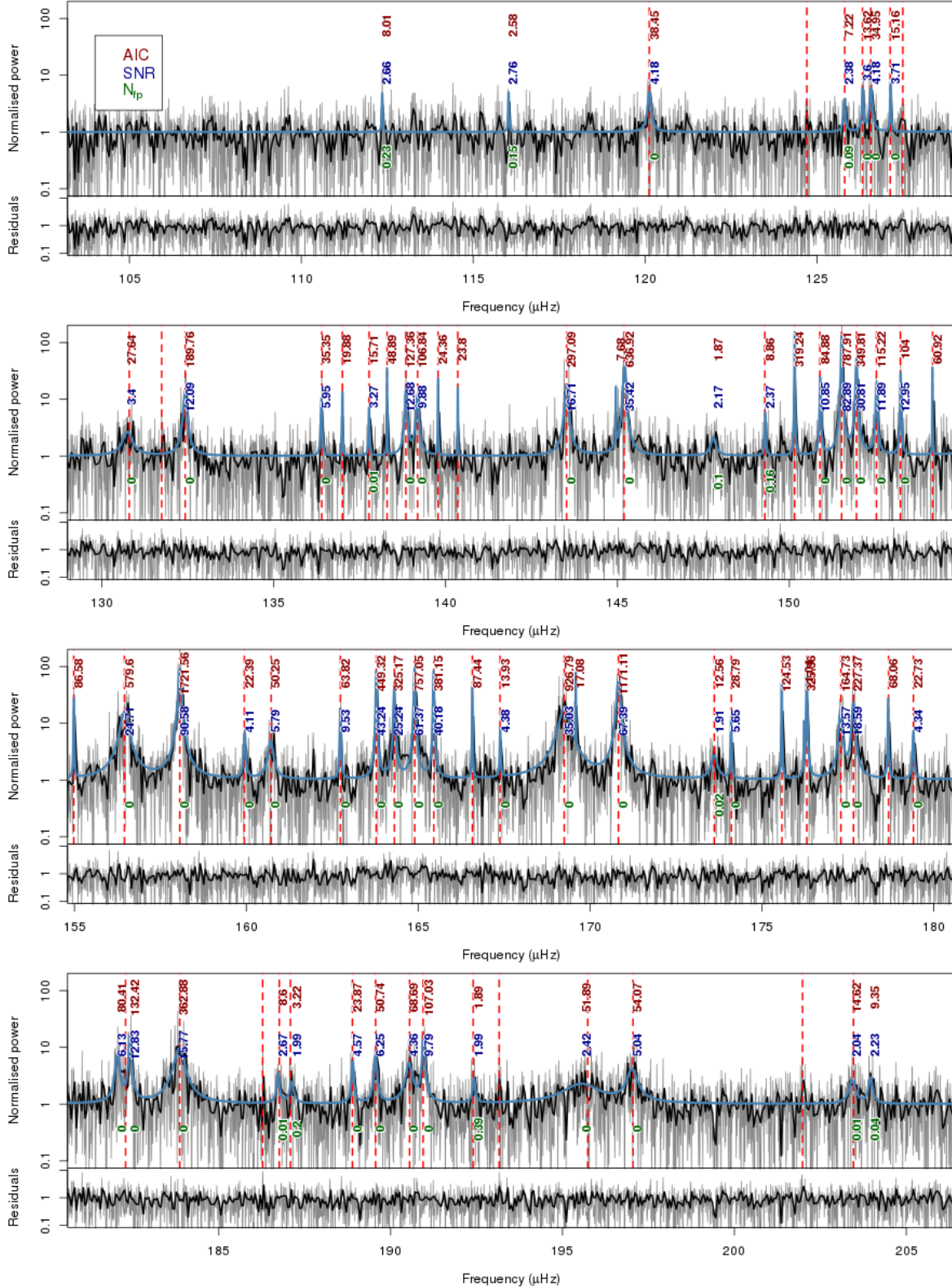


Figure 15. Background-normalised PDS (grey) for *Kepler* target KIC 12008916 with a 0.05 μHz binned version (black) in the region where the solar-like oscillations are located. The vertical red lines are placed at the frequencies of the oscillation modes obtained by Corsaro et al. (2015) with a detection probability greater than 0.9. The blue line is an MLE fit using the heights, locations and line widths obtained with the peak detection results as input parameters to build a PDS model. We also indicate the AIC difference with the null hypothesis model (red), the SNR (blue) and N_{fp} (green) as described in Section 3 for each oscillation. The residuals are calculated by dividing the background-normalised PDS by the fitted model.

ues for the white noise and granulation background are reported in Table A1 and for the power excess in Table A2. The expected value for each parameter is estimated by the median of the posterior density function while the lower and upper uncertainties are estimated as the 18 and 64 percentiles of the posterior density function.

APPENDIX B: RESULTS FOR THE OSCILLATION MODES

We applied the peak finding procedure to the 19 red-giant stars analysed by Corsaro et al. (2015) as described in Section 6. We then used the identified peaks as initial values for a parameter optimisation using MLE. When fitting a Lorentzian profile in a PDS the height and line width show high correlations which could hinder the MLE optimisation. For this reason it is more stable to use optimise the amplitude instead of the height. That is, during the MLE optimisation each Lorentzian profile is described by

$$O_k^{\text{resolved}} = \frac{A_k^2}{\pi\gamma_k \left[1 + \left(\frac{\nu - \nu_k}{\gamma_k} \right)^2 \right]} \quad (\text{B1})$$

where $A_k = \sqrt{\pi I_k \gamma_k}$ is the amplitude of a Lorentzian profile centered at ν_k , with height I_k and half-width at half-maximum γ_k .

We described the unresolved oscillations in a PDS having frequency resolution of $\delta\nu$ as

$$O_k^{\text{unresolved}} = H_k \text{sinc}^2 \left(\frac{\nu - \nu_k}{\delta\nu} \right) \quad (\text{B2})$$

where H_k is the height and ν_k is the location of the oscillation. The unresolved oscillations are detected by identified single points in the PDS with a false-alarm probability lower than 10^{-4} . When a significant oscillation is detected in this way it is fitted with both Eq. B1 and B2 and the model with the lower AIC is chosen. If model B1 is preferred, it is reported as a resolved oscillation, however, the SNR value is missing in the table.

In the following tables we report the obtained parameters for the resolved and unresolved oscillations using Eqs. (B1) and (B2) respectively. The uncertainties are derived from the covariance matrix as estimated by the inverse of the Hessian matrix evaluated at the MLE. The reported AIC value corresponds to the difference in AIC between a PDS model having and omitting that oscillation.

Table A1. Estimated PDS fit parameters for the white noise and granulation background in the 19 red-giant stars analysed by Corsaro et al. (2015) using Eq. 9. The estimated parameter value is the median of the posterior distribution. The lower and upper uncertainties for each parameter are the 16 and 84 percentiles of its posterior distribution.

KIC	P_n (ppm ² /μHz)	A_1 (ppm ² /μHz)	b_1 (μHz)	A_2 (ppm ² /μHz)	b_2 (μHz)	A_3 (ppm ² /μHz)	b_3 (μHz)
3744043	$8.23^{+0.20}_{-0.22} \times 10^0$	$1.73^{+0.06}_{-0.05} \times 10^3$	$2.41^{+0.06}_{-0.06} \times 10^1$	$3.00^{+0.27}_{-0.74} \times 10^2$	$9.44^{+0.24}_{-0.52} \times 10^1$	$3.73^{+8.47}_{-2.58} \times 10^1$	$1.10^{+0.18}_{-0.08} \times 10^2$
6117517	$1.20^{+0.03}_{-0.03} \times 10^1$	$4.03^{+0.66}_{-0.56} \times 10^3$	$1.77^{+0.26}_{-0.22} \times 10^0$	$1.67^{+0.06}_{-0.05} \times 10^3$	$2.94^{+0.07}_{-0.07} \times 10^1$	$4.01^{+0.13}_{-0.14} \times 10^2$	$1.04^{+0.01}_{-0.01} \times 10^2$
6144777	$1.05^{+0.03}_{-0.03} \times 10^1$	$4.06^{+0.61}_{-0.56} \times 10^3$	$1.32^{+0.15}_{-0.13} \times 10^0$	$1.16^{+0.04}_{-0.03} \times 10^3$	$3.31^{+0.08}_{-0.08} \times 10^1$	$2.67^{+0.09}_{-0.09} \times 10^2$	$1.20^{+0.02}_{-0.02} \times 10^2$
7060732	$3.12^{+0.07}_{-0.07} \times 10^1$	$8.03^{+1.12}_{-0.99} \times 10^3$	$1.86^{+0.23}_{-0.19} \times 10^0$	$1.07^{+0.04}_{-0.04} \times 10^3$	$3.14^{+0.08}_{-0.08} \times 10^1$	$2.60^{+0.10}_{-0.09} \times 10^2$	$1.18^{+0.03}_{-0.03} \times 10^2$
7619745	$1.78^{+0.11}_{-0.10} \times 10^1$	$3.60^{+0.52}_{-0.44} \times 10^3$	$1.23^{+0.11}_{-0.10} \times 10^0$	$5.46^{+0.13}_{-0.13} \times 10^2$	$4.31^{+0.08}_{-0.08} \times 10^1$	$1.14^{+0.04}_{-0.04} \times 10^2$	$1.70^{+0.06}_{-0.06} \times 10^2$
8366239	$1.98^{+0.15}_{-0.18} \times 10^1$	$1.68^{+0.22}_{-0.19} \times 10^3$	$2.18^{+0.24}_{-0.22} \times 10^0$	$4.07^{+0.11}_{-0.11} \times 10^2$	$4.69^{+0.11}_{-0.11} \times 10^1$	$9.64^{+0.13}_{-0.13} \times 10^1$	$1.77^{+0.13}_{-0.12} \times 10^2$
8475025	$2.49^{+0.05}_{-0.05} \times 10^1$	$1.76^{+0.22}_{-0.18} \times 10^4$	$1.34^{+0.08}_{-0.08} \times 10^0$	$1.55^{+0.05}_{-0.05} \times 10^3$	$2.81^{+0.07}_{-0.07} \times 10^1$	$3.33^{+0.13}_{-0.13} \times 10^2$	$1.03^{+0.02}_{-0.02} \times 10^2$
8718745	$2.10^{+0.06}_{-0.06} \times 10^1$	$9.19^{+1.14}_{-0.97} \times 10^4$	$1.08^{+0.06}_{-0.06} \times 10^0$	$1.57^{+0.05}_{-0.05} \times 10^3$	$3.03^{+0.07}_{-0.07} \times 10^1$	$3.05^{+0.10}_{-0.10} \times 10^2$	$1.19^{+0.02}_{-0.02} \times 10^2$
9145955	$7.96^{+0.25}_{-0.26} \times 10^0$	$4.84^{+0.55}_{-0.45} \times 10^3$	$2.16^{+0.15}_{-0.15} \times 10^0$	$8.52^{+0.27}_{-0.27} \times 10^2$	$3.33^{+0.08}_{-0.08} \times 10^1$	$2.00^{+0.08}_{-0.07} \times 10^2$	$1.15^{+0.02}_{-0.02} \times 10^2$
9267654	$2.20^{+0.04}_{-0.04} \times 10^1$	$5.12^{+0.74}_{-0.66} \times 10^3$	$1.28^{+0.12}_{-0.10} \times 10^0$	$9.87^{+0.31}_{-0.31} \times 10^2$	$2.95^{+0.07}_{-0.07} \times 10^1$	$2.47^{+0.09}_{-0.09} \times 10^2$	$1.05^{+0.02}_{-0.02} \times 10^2$
9475697	$1.50^{+0.03}_{-0.03} \times 10^1$	$2.00^{+0.07}_{-0.07} \times 10^3$	$2.60^{+0.08}_{-0.08} \times 10^1$	$3.04^{+0.31}_{-0.72} \times 10^2$	$9.61^{+0.08}_{-0.97} \times 10^1$	$1.05^{+0.09}_{-0.65} \times 10^2$	$1.08^{+0.08}_{-0.05} \times 10^2$
9882316	$1.60^{+0.17}_{-0.19} \times 10^1$	$1.88^{+0.22}_{-0.19} \times 10^3$	$1.99^{+0.18}_{-0.16} \times 10^0$	$3.72^{+0.09}_{-0.09} \times 10^2$	$4.53^{+0.09}_{-0.09} \times 10^1$	$8.20^{+0.23}_{-0.24} \times 10^1$	$2.10^{+0.11}_{-0.11} \times 10^2$
10123207	$2.16^{+0.10}_{-0.10} \times 10^1$	$9.36^{+1.24}_{-1.07} \times 10^3$	$1.06^{+0.08}_{-0.08} \times 10^0$	$8.84^{+0.23}_{-0.24} \times 10^2$	$3.83^{+0.08}_{-0.08} \times 10^1$	$1.86^{+0.06}_{-0.06} \times 10^2$	$1.55^{+0.04}_{-0.04} \times 10^2$
10200377	$2.61^{+0.07}_{-0.07} \times 10^1$	$7.52^{+1.00}_{-0.87} \times 10^3$	$1.37^{+0.14}_{-0.10} \times 10^0$	$8.77^{+0.27}_{-0.27} \times 10^2$	$3.54^{+0.09}_{-0.09} \times 10^1$	$2.25^{+0.10}_{-0.10} \times 10^2$	$1.17^{+0.03}_{-0.03} \times 10^2$
10257278	$2.92^{+0.09}_{-0.09} \times 10^1$	$5.75^{+0.73}_{-0.73} \times 10^3$	$1.05^{+0.10}_{-0.09} \times 10^0$	$9.58^{+0.29}_{-0.29} \times 10^2$	$3.61^{+0.09}_{-0.09} \times 10^1$	$2.27^{+0.08}_{-0.08} \times 10^2$	$1.36^{+0.04}_{-0.04} \times 10^2$
11353313	$2.44^{+0.05}_{-0.05} \times 10^1$	$7.63^{+1.04}_{-0.88} \times 10^3$	$1.36^{+0.12}_{-0.11} \times 10^0$	$9.74^{+0.31}_{-0.30} \times 10^2$	$3.17^{+0.08}_{-0.07} \times 10^1$	$2.24^{+0.08}_{-0.08} \times 10^2$	$1.13^{+0.02}_{-0.02} \times 10^2$
11913545	$2.39^{+0.05}_{-0.05} \times 10^1$	$2.05^{+0.06}_{-0.06} \times 10^3$	$2.63^{+0.06}_{-0.06} \times 10^1$	$3.51^{+0.31}_{-0.86} \times 10^2$	$1.04^{+0.02}_{-0.02} \times 10^2$	$8.88^{+8.99}_{-5.05} \times 10^1$	$1.14^{+0.09}_{-0.03} \times 10^2$
11968334	$2.92^{+0.08}_{-0.08} \times 10^1$	$7.60^{+0.88}_{-0.88} \times 10^3$	$1.16^{+0.08}_{-0.08} \times 10^0$	$9.92^{+0.27}_{-0.27} \times 10^2$	$3.62^{+0.07}_{-0.07} \times 10^1$	$2.17^{+0.07}_{-0.07} \times 10^2$	$1.42^{+0.03}_{-0.03} \times 10^2$
12008916	$2.04^{+0.11}_{-0.11} \times 10^1$	$1.31^{+0.18}_{-0.16} \times 10^4$	$1.06^{+0.07}_{-0.07} \times 10^0$	$7.31^{+0.19}_{-0.18} \times 10^2$	$4.11^{+0.08}_{-0.09} \times 10^1$	$1.61^{+0.05}_{-0.05} \times 10^2$	$1.62^{+0.05}_{-0.05} \times 10^2$

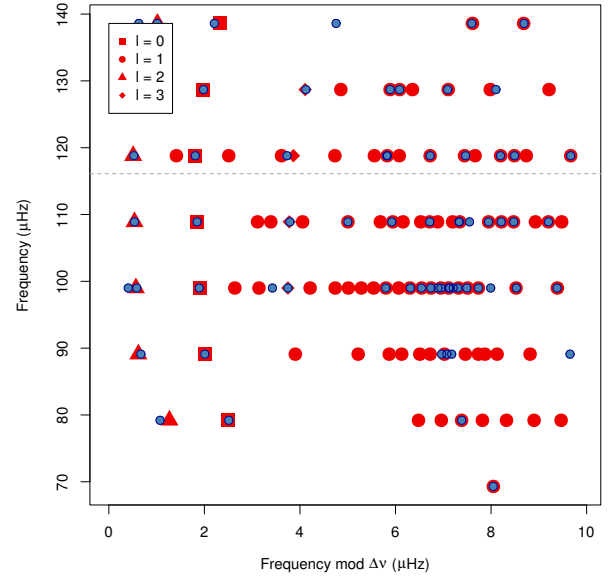
Table A2. Same as Table A1 for the oscillations power excess parameters.

KIC	P_g (ppm ² /μHz)	ν_{\max} (μHz)	σ_{env} (μHz)
3744043	$5.28^{+0.15}_{-0.14} \times 10^2$	$1.125^{+0.003}_{-0.003} \times 10^2$	$1.21^{+0.03}_{-0.03} \times 10^1$
6117517	$6.14^{+0.17}_{-0.17} \times 10^2$	$1.203^{+0.003}_{-0.003} \times 10^2$	$1.33^{+0.03}_{-0.03} \times 10^1$
6144777	$5.65^{+0.15}_{-0.15} \times 10^2$	$1.297^{+0.003}_{-0.003} \times 10^2$	$1.27^{+0.03}_{-0.03} \times 10^1$
7060732	$4.23^{+0.13}_{-0.13} \times 10^2$	$1.323^{+0.003}_{-0.003} \times 10^2$	$1.27^{+0.04}_{-0.03} \times 10^1$
7619745	$2.17^{+0.06}_{-0.06} \times 10^2$	$1.707^{+0.004}_{-0.004} \times 10^2$	$1.49^{+0.04}_{-0.04} \times 10^1$
8366239	$1.43^{+0.05}_{-0.04} \times 10^2$	$1.857^{+0.005}_{-0.005} \times 10^2$	$1.69^{+0.07}_{-0.07} \times 10^1$
8475025	$5.81^{+0.17}_{-0.18} \times 10^2$	$1.129^{+0.003}_{-0.003} \times 10^2$	$1.09^{+0.03}_{-0.03} \times 10^1$
8718745	$5.72^{+0.17}_{-0.16} \times 10^2$	$1.296^{+0.003}_{-0.003} \times 10^2$	$1.15^{+0.03}_{-0.03} \times 10^1$
9145955	$2.84^{+0.07}_{-0.07} \times 10^2$	$1.320^{+0.004}_{-0.004} \times 10^2$	$1.50^{+0.04}_{-0.03} \times 10^1$
9267654	$4.65^{+0.14}_{-0.13} \times 10^2$	$1.184^{+0.003}_{-0.003} \times 10^2$	$1.14^{+0.03}_{-0.03} \times 10^1$
9475697	$5.82^{+0.13}_{-0.16} \times 10^2$	$1.150^{+0.003}_{-0.003} \times 10^2$	$1.29^{+0.04}_{-0.03} \times 10^1$
9882316	$1.06^{+0.04}_{-0.04} \times 10^2$	$1.823^{+0.005}_{-0.005} \times 10^2$	$1.52^{+0.07}_{-0.07} \times 10^1$
10123207	$4.46^{+0.12}_{-0.12} \times 10^2$	$1.607^{+0.003}_{-0.003} \times 10^2$	$1.26^{+0.03}_{-0.03} \times 10^1$
10200377	$3.56^{+0.09}_{-0.09} \times 10^2$	$1.433^{+0.003}_{-0.003} \times 10^2$	$1.47^{+0.04}_{-0.03} \times 10^1$
10257278	$4.11^{+0.12}_{-0.12} \times 10^2$	$1.503^{+0.003}_{-0.003} \times 10^2$	$1.24^{+0.04}_{-0.04} \times 10^1$
11353313	$3.75^{+0.11}_{-0.10} \times 10^2$	$1.264^{+0.003}_{-0.003} \times 10^2$	$1.25^{+0.03}_{-0.03} \times 10^1$
11913545	$7.85^{+0.26}_{-0.24} \times 10^2$	$1.173^{+0.003}_{-0.003} \times 10^2$	$1.08^{+0.03}_{-0.03} \times 10^1$
11968334	$4.55^{+0.15}_{-0.14} \times 10^2$	$1.413^{+0.003}_{-0.003} \times 10^2$	$1.10^{+0.02}_{-0.02} \times 10^1$
12008916	$3.02^{+0.08}_{-0.08} \times 10^2$	$1.613^{+0.004}_{-0.003} \times 10^2$	$1.49^{+0.04}_{-0.04} \times 10^1$

ν_k	A_k	γ_k	SNR	AIC
77.346±0.013	0.408±0.117	0.016±0.013	2.23	5.58
80.273±0.016	0.424±0.113	0.02±0.015	2.24	5.35
81.711±0.02	0.888±0.118	0.051±0.018	6.30	59.13
86.586±0.005	0.735±0.174	0.009±0.006	9.09	62.09
89.771±0.036	0.919±0.121	0.107±0.045	3.87	42.59
91.109±0.014	1.323±0.147	0.048±0.015	11.96	178.70
96.065±0.142	1.458±0.182	0.4±0.158	2.08	25.66
96.276±0.192	1.528±0.168	0.4±0.108	2.90	30.72
98.752±0.014	0.426±0.128	0.016±0.014	5.56	3.28
99.406±0.037	1.203±0.201	0.104±0.06	2.52	44.72
99.585±0.011	1.456±0.219	0.027±0.012	6.70	97.67
100.892±0.011	2.43±0.242	0.045±0.012	19.33	782.22
102.424±0.005	0.283±0.071	0.01±NaN	42.01	3.54
102.749±0.009	0.587±0.138	0.015±0.013	1.91	23.72
104.797±0.006	0.538±0.153	0.008±0.006	4.42	19.86
105.311±0.008	0.827±0.168	0.016±0.011	5.56	43.82
105.544±0.008	1.185±0.208	0.017±0.008	8.23	104.40
105.743±0.004	0.802±0.267	0.006±0.006	16.51	31.28
106.11±0.004	1.438±0.428	0.005±0.004		51.76
106.207±0.067	1.531±0.186	0.249±0.112		40.17
106.492±0.014	0.537±0.171	0.013±0.01	5.43	1.67
109.437±0.015	3.392±0.254	0.081±0.016	59.91	1315.23
110.746±0.013	3.926±0.311	0.068±0.014	88.56	1936.95
112.688±0.013	0.999±0.169	0.035±0.029	5.73	77.42
114.824±0.008	1.174±0.195	0.02±0.01	15.76	102.34
115.617±0.016	3.089±0.224	0.092±0.019	45.39	1071.80
116.228±0.058	1.017±0.237	0.094±0.082		2.37
116.237±0.003	1.956±0.608	0.005±0.004		107.30
116.448±0.01	0.55±0.171	0.011±0.01	4.96	4.80
117.112±0.005	0.757±0.208	0.007±0.005	10.38	51.62
117.376±0.007	0.489±0.152	0.006±0.005	5.08	15.39
119.324±0.018	2.807±0.195	0.105±0.021	36.71	846.37
120.609±0.011	3.423±0.309	0.053±0.012	76.99	1464.76
122.528±0.052	1.184±0.122	0.175±0.051	5.35	65.47
125.524±0.015	2.139±0.188	0.068±0.017	26.29	470.58
126.266±0.02	1.623±0.152	0.081±0.024	12.72	204.09
126.997±0.011	0.517±0.133	0.015±0.011	3.65	10.76
127.292±0.009	0.744±0.151	0.015±0.007	7.92	43.37
129.403±0.022	2.303±0.163	0.12±0.025	22.12	487.64
130.681±0.031	2.164±0.141	0.177±0.034	15.18	380.50
132.825±0.022	0.586±0.119	0.038±0.022	2.92	13.20
134.588±0.019	0.585±0.127	0.034±0.023	2.71	12.91
134.786±0.004	0.449±0.169	0.005±0.007	4.06	12.18
135.793±0.03	1.626±0.13	0.145±0.036	9.96	195.09
136.802±0.052	1.155±0.126	0.173±0.054	4.12	56.87
139.227±0.015	0.625±0.132	0.028±0.019	3.32	17.78
139.613±0.018	0.848±0.143	0.045±0.029	5.08	39.21
140.808±0.092	1.452±0.126	0.398±0.103	3.48	89.35
143.357±0.023	0.43±0.129	0.033±0.031	1.50	2.38
146.199±0.043	1.075±0.116	0.143±0.044	5.20	60.98
147.289±0.027	0.713±0.117	0.057±0.025	3.67	23.13
149.464±0.253	0.972±0.182	0.4±0.197	1.23	17.38
150.781±0.015	0.351±0.158	0.018±0.034	1.62	0.13
156.702±0.106	0.619±0.157	0.164±0.13	1.54	4.44

Table B1. Resolved oscillations for KIC 3744043 .

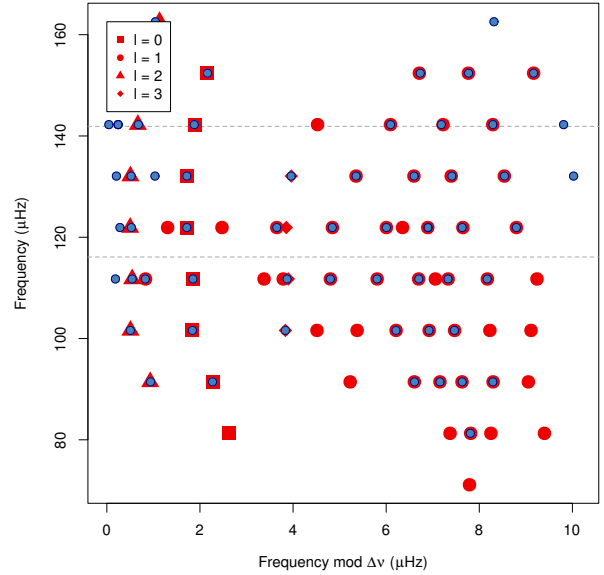
ν_k	H_k	AIC
105.89±0.002	32.931±31.542	9.79
105.951±0.002	69.363±51.538	17.41
106.737±0.002	63.729±46.161	36.35
107.529±0.002	84.342±43.169	82.07
108.382±0.002	37.01±23.872	23.61
113.904±0.001	50.605±40.142	63.95
116.848±0.002	84.986±46.947	54.30
118.102±0.001	31.681±21.444	41.29
124.615±0.003	49.973±56.838	0.73
124.632±0.002	172.94±93.903	133.71
128.467±0.002	52.997±34.592	53.68

Table B2. Unresolved oscillations for KIC 3744043 .**Figure B1.** Same as Fig. 14 for KIC 3744043.

ν_k	A_k	γ_k	SNR	AIC
67.114±0.018	0.423±0.148	0.023±0.034	1.52	4.72
68.496±0.038	0.466±0.123	0.053±0.04	1.65	2.85
89.088±0.01	0.718±0.132	0.021±0.011	5.64	44.86
92.379±0.005	0.642±0.18	0.007±0.007	4.85	44.95
93.71±0.038	1.073±0.115	0.124±0.039	5.36	69.58
98.595±0.006	0.929±0.184	0.013±0.007	12.17	103.93
99.073±0.005	0.674±0.174	0.008±0.006	6.96	47.59
99.733±0.004	0.39±0.139	0.005±0.006	3.74	15.38
102.106±0.019	1.342±0.134	0.076±0.025	9.13	162.09
103.439±0.012	1.845±0.191	0.045±0.013	23.81	428.76
105.436±0.011	0.598±0.123	0.019±0.011	4.42	25.05
108.522±0.007	1.747±0.271	0.018±0.007		437.74
111.945±0.008	0.712±0.168	0.012±0.008	7.28	28.29
112.303±0.012	2.027±0.207	0.047±0.013	26.24	467.97
112.587±0.009	0.766±0.193	0.013±0.012	6.69	24.81
113.609±0.007	4.115±0.552	0.023±0.007	170.47	2740.04
115.631±0.016	1.344±0.143	0.053±0.015	12.53	176.63
118.462±0.01	2.416±0.252	0.042±0.013		716.29
122.202±0.028	1.265±0.176	0.081±0.036	8.98	46.52
122.447±0.011	2.094±0.241	0.038±0.012	31.57	286.86
123.638±0.012	3.807±0.304	0.067±0.014	92.30	2062.10
128.819±0.01	2.479±0.3	0.032±0.01	30.28	350.33
128.819±0.212	1.276±0.237	0.4±0.436		7.46
132.603±0.021	2.167±0.166	0.108±0.026	19.06	411.98
133.799±0.018	2.805±0.199	0.098±0.019	36.20	891.32
136.039±0.018	0.869±0.124	0.046±0.019	6.11	51.31
138.681±0.015	1.37±0.152	0.049±0.016	12.82	174.16
139.492±0.017	1.681±0.155	0.067±0.017	16.75	286.89
140.623±0.011	0.725±0.136	0.023±0.013	5.40	38.15
142.105±0.015	0.425±0.128	0.015±0.012	2.95	3.30
142.284±0.01	0.503±0.141	0.013±0.01	3.81	8.00
142.917±0.032	1.534±0.142	0.132±0.039	2.84	148.52
144.119±0.053	1.86±0.131	0.276±0.058	6.88	244.22
148.335±0.007	0.74±0.162	0.012±0.008	7.51	50.23
149.425±0.043	1.357±0.118	0.169±0.041	6.50	113.10
150.532±0.044	0.985±0.121	0.116±0.041	4.69	44.61
152.051±0.006	0.327±0.36	0.005±0.02	1.77	4.66
153.581±0.326	1.423±0.216	0.4±0.231	2.78	74.05
159.132±0.027	0.576±0.118	0.045±0.025	3.15	10.95
160.169±0.056	1.144±0.116	0.192±0.054	4.51	64.30
161.566±0.018	0.515±0.122	0.028±0.021	2.43	9.73
163.604±0.102	1.002±0.131	0.306±0.115	2.65	28.46
170.876±0.064	0.721±0.13	0.127±0.071	2.49	15.07

Table B3. Resolved oscillations for KIC 6117517 .

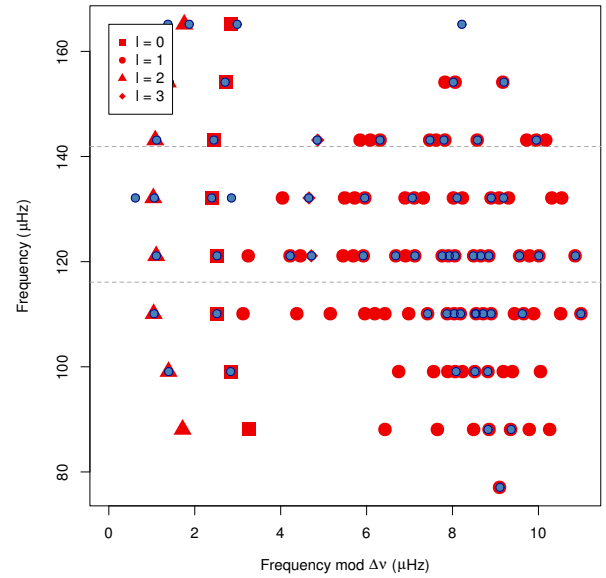
ν_k	H_k	AIC
98.05±0.002	117.084±59.233	101.87
107.811±0.002	97.1±51.656	116.98
109.066±0.001	726.76±234.549	398.68
116.561±0.002	31.435±28.226	46.70
117.565±0.001	123.591±84.557	248.40
119.089±0.001	4803.886±1292.46	990.16
119.93±0.001	353.564±164.366	346.94
125.57±0.001	44.673±45.806	65.45
126.763±0.001	73.775±52.275	95.38
127.926±0.001	334.899±146.307	427.70
129.553±0.001	1054.725±327.149	238.62
130.716±0.001	164.473±74.261	172.81
132.286±0.002	81.004±61.568	37.35
133.114±0.002	39.786±38.407	22.61
137.434±0.001	93.987±54.975	120.10

Table B4. Unresolved oscillations for KIC 6117517 .**Figure B2.** Same as Fig. 14 for KIC 6117517.

ν_k	A_k	γ_k	SNR	AIC
86.174±0.046	0.587±0.159	0.09±0.093	1.94	7.44
96.907±0.042	0.756±0.174	0.116±0.112	2.26	19.81
97.445±0.005	0.314±0.141	0.005±0.011	1.65	1.50
100.483±0.032	0.55±0.118	0.054±0.033	1.92	8.64
101.924±0.014	1.048±0.136	0.042±0.018	8.07	102.77
107.172±0.067	1.132±0.145	0.214±0.081	1.53	45.56
107.612±0.02	1.036±0.144	0.056±0.025	6.15	52.97
107.91±0.011	0.603±0.143	0.017±0.012	4.39	15.87
111.153±0.028	1.547±0.127	0.123±0.03	10.46	196.01
112.615±0.014	1.986±0.179	0.063±0.016	23.50	463.93
117.969±0.011	1.061±0.184	0.024±0.013	9.96	47.57
118.137±0.011	1.617±0.232	0.029±0.013	18.86	142.17
118.285±0.012	1.18±0.197	0.028±0.016	12.04	52.85
118.815±0.004	0.649±0.208	0.005±0.006	4.94	39.34
119.726±0.059	1.103±0.137	0.211±0.084	2.83	46.86
122.216±0.017	2.774±0.197	0.098±0.02	37.63	899.51
123.628±0.007	4.25±0.516	0.027±0.008	160.61	2701.71
125.331±0.006	0.659±0.164	0.009±0.006	7.05	36.59
125.83±0.011	1.42±0.173	0.035±0.012	16.43	223.09
128.871±0.011	1.703±0.223	0.034±0.017	29.02	200.76
129.035±0.007	1.586±0.3	0.015±0.008	29.20	96.59
129.17±0.009	1.438±0.238	0.02±0.009	17.22	109.46
129.768±0.004	1.73±0.385	0.007±0.004	37.64	293.47
131.968±0.006	0.623±0.167	0.007±0.005	7.45	31.43
133.179±0.012	3.737±0.311	0.062±0.013	82.74	1872.07
134.515±0.009	3.849±0.391	0.04±0.01	116.97	2015.89
136.774±0.024	1.091±0.126	0.077±0.027	6.64	77.91
139.183±0.032	1.632±0.135	0.144±0.036	9.48	162.19
140.225±0.018	2.701±0.196	0.096±0.019	34.41	745.62
141.307±0.037	1.361±0.134	0.112±0.028	9.23	98.89
144.243±0.028	2.32±0.151	0.167±0.034	18.45	429.31
145.574±0.021	2.921±0.187	0.126±0.023	34.80	880.38
147.979±0.022	0.772±0.126	0.052±0.027	3.93	31.44
149.441±0.012	0.552±0.136	0.016±0.015	3.74	18.05
150.603±0.021	1.052±0.14	0.056±0.023	5.92	68.21
150.93±0.028	0.789±0.145	0.059±0.033	2.77	19.62
151.712±0.023	1.797±0.139	0.112±0.025	14.07	298.66
153.082±0.003	0.554±0.191	0.005±0.007	3.60	33.31
154.858±0.005	0.383±0.167	0.005±0.012	1.97	4.23
155.544±0.027	1.614±0.132	0.13±0.034	10.20	202.76
156.846±0.035	1.566±0.126	0.17±0.043	8.19	169.60
162.159±0.041	1.329±0.117	0.17±0.043	6.40	110.27
163.337±0.023	0.986±0.122	0.067±0.024	5.93	63.46
167.021±0.145	1.075±0.162	0.325±0.18	1.70	28.86
168.136±0.23	1.026±0.158	0.397±0.208	1.91	20.36
173.367±0.038	0.689±0.186	0.098±0.117	2.28	15.20

Table B5. Resolved oscillations for KIC 6144777 .

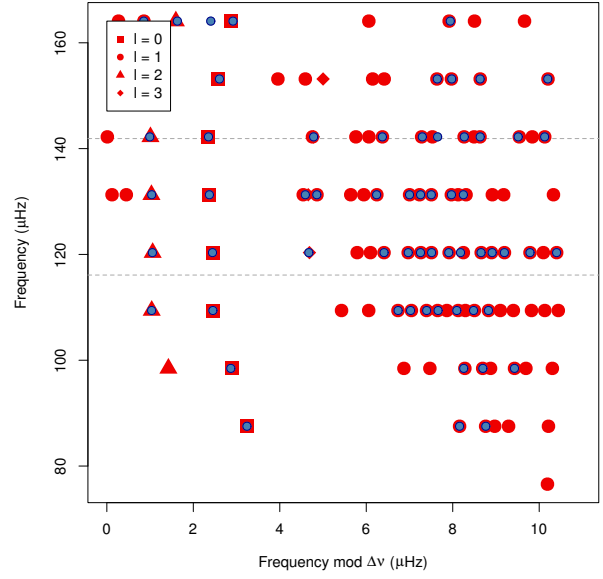
ν_k	H_k	AIC
117.521±0.002	45.826±26.688	51.09
118.626±0.002	76.016±66.075	4.94
118.648±0.002	161.22±133.998	36.62
118.997±0.002	144.317±73.789	98.76
121.087±0.002	34.776±21.847	31.75
127.034±0.001	65.586±51.112	68.83
127.786±0.002	53.426±38.098	56.73
128.236±0.002	234.129±135.883	109.43
129.594±0.001	1339.976±639.958	158.25
129.955±0.001	625.488±293.78	324.77
130.668±0.001	88.336±54.587	90.59
131.119±0.002	203.146±124.72	160.28
132.738±0.001	132.713±93.244	87.96
134.974±0.002	37.783±28.857	16.03
138.077±0.001	38.795±26.616	43.53
141.021±0.002	101.514±63.871	40.41

Table B6. Unresolved oscillations for KIC 6144777 .**Figure B3.** Same as Fig. 14 for KIC 6144777.

ν_k	A_k	γ_k	SNR	AIC
90.76±0.015	0.557±0.116	0.027±0.017	2.96	17.64
95.679±0.004	0.364±0.152	0.005±0.011	2.25	6.26
96.285±0.015	0.384±0.113	0.018±0.015	1.88	2.81
101.327±0.03	0.893±0.112	0.077±0.026	5.25	48.70
106.715±0.039	1.158±0.125	0.157±0.059	5.31	78.31
107.157±0.004	0.371±0.156	0.005±0.011	2.95	3.13
107.888±0.008	0.34±0.118	0.007±0.006	2.78	4.48
110.436±0.013	0.893±0.133	0.031±0.013	7.34	70.40
111.853±0.011	1.515±0.173	0.04±0.013	17.48	273.88
116.137±0.005	0.441±0.197	0.005±0.009	3.19	8.62
117.494±0.067	1.845±0.14	0.352±0.085	9.10	166.72
117.882±0.021	0.934±0.22	0.012±0.016	13.54	29.64
121.393±0.016	2.162±0.175	0.077±0.017	26.08	540.98
122.784±0.012	2.296±0.214	0.054±0.014	34.13	657.91
125.012±0.017	0.914±0.127	0.044±0.019	6.33	62.66
127.595±0.011	0.652±0.137	0.019±0.012	4.98	24.11
128.248±0.006	1.769±0.384	0.012±0.007	36.98	135.94
128.52±0.023	2.131±0.177	0.094±0.024	27.33	394.78
128.995±0.005	1.416±0.283	0.011±0.005	28.33	165.37
129.251±0.004	0.852±0.261	0.006±0.005	11.78	55.16
129.535±0.011	0.664±0.13	0.022±0.014	5.41	26.64
130.127±0.004	0.524±0.171	0.005±0.007	2.81	33.41
132.318±0.016	2.794±0.208	0.089±0.019	44.14	907.93
133.652±0.011	3.22±0.304	0.048±0.011	70.62	1387.90
135.871±0.019	0.807±0.129	0.041±0.02	4.79	39.91
136.136±0.013	0.659±0.151	0.023±0.022	3.72	24.39
137.52±0.004	0.428±0.185	0.005±0.01	3.37	18.18
138.536±0.01	0.745±0.151	0.017±0.009	7.14	31.69
138.785±0.005	1.823±0.397	0.01±0.005	47.03	337.63
139.251±0.011	1.78±0.269	0.027±0.012		114.58
139.526±0.019	2.433±0.21	0.082±0.021	32.36	460.81
143.213±0.026	2.199±0.146	0.155±0.034	18.71	454.72
144.571±0.012	2.437±0.224	0.055±0.014	38.33	704.79
147.003±0.019	0.712±0.119	0.041±0.02	4.30	30.12
148.593±0.004	0.361±0.147	0.005±0.008	3.18	5.89
149.517±0.011	0.678±0.155	0.02±0.016	4.96	19.68
149.87±0.036	1.352±0.134	0.139±0.043	4.04	105.37
150.488±0.011	1.274±0.182	0.031±0.016	15.07	117.68
150.855±0.019	1.235±0.151	0.062±0.027	8.74	98.20
151.735±0.014	0.499±0.121	0.02±0.015	3.32	9.93
152.346±0.005	0.494±0.178	0.005±0.008	1.84	20.15
154.316±0.048	1.58±0.127	0.243±0.067	6.40	149.86
155.764±0.042	1.295±0.125	0.161±0.05	5.82	91.76
160.803±0.029	0.597±0.137	0.05±0.038	2.05	9.41
161.138±0.024	0.806±0.126	0.051±0.023	4.13	31.51
161.793±0.042	1.026±0.121	0.123±0.045	3.88	52.31
163.358±0.028	0.464±0.114	0.033±0.02	2.32	4.26
164.954±0.007	0.389±0.144	0.007±0.009	2.77	4.75
165.731±0.08	1.018±0.131	0.23±0.085	2.01	35.84
167.018±0.034	0.825±0.142	0.088±0.053	2.76	33.22
172.043±0.006	0.312±0.131	0.005±0.014	1.82	2.90
177.148±0.051	0.617±0.172	0.089±0.102	1.91	10.00

Table B7. Resolved oscillations for KIC 7060732 .

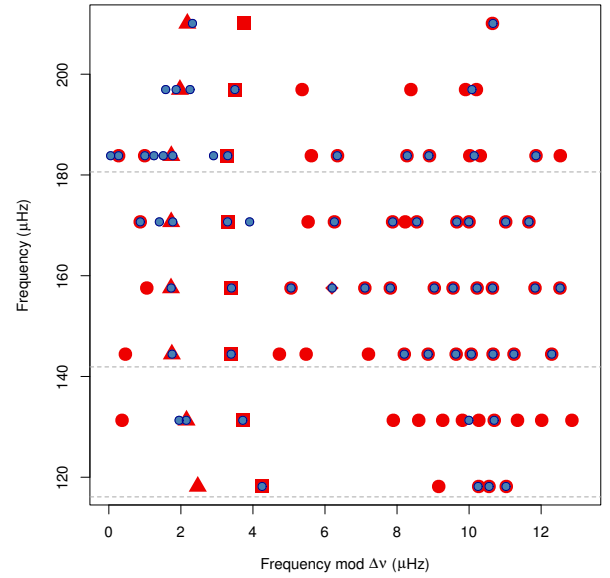
ν_k	H_k	AIC
116.797±0.002	70.56±45.876	40.42
118.225±0.002	96.389±58.644	36.66
126.752±0.001	81.066±49.444	95.79
127.311±0.001	179.366±104.066	258.20
127.852±0.001	211.069±162.818	246.88
130.743±0.002	46.288±47.778	66.49
138.281±0.001	149.966±100.648	132.00

Table B8. Unresolved oscillations for KIC 7060732 .**Figure B4.** Same as Fig. 14 for KIC 7060732.

ν_k	A_k	γ_k	SNR	AIC
122.424±0.049	0.546±0.125	0.075±0.05	1.76	5.99
128.42±0.018	0.486±0.16	0.013±0.022	3.24	14.07
128.725±0.01	0.545±0.123	0.017±0.012	3.18	18.87
129.195±0.023	0.49±0.117	0.029±0.021	2.37	8.58
133.25±0.005	0.472±0.171	0.005±0.007	4.31	15.57
133.449±0.019	0.557±0.126	0.036±0.028	1.87	12.72
135.018±0.028	1.124±0.117	0.095±0.028	6.41	91.69
141.295±0.084	1.143±0.121	0.29±0.085	4.29	49.88
146.186±0.041	1.325±0.116	0.168±0.043	6.53	112.06
147.825±0.012	1.852±0.194	0.044±0.012	24.19	431.27
153.294±0.004	0.395±0.143	0.005±0.011	2.49	14.16
154.06±0.018	1.04±0.129	0.054±0.02	6.46	85.43
154.493±0.006	1.399±0.269	0.012±0.006	26.59	250.01
155.094±0.013	0.964±0.137	0.035±0.015	7.42	81.65
155.672±0.007	0.739±0.155	0.013±0.007	7.81	53.24
159.29±0.015	2.013±0.173	0.071±0.018	23.65	470.41
160.964±0.009	3.199±0.342	0.037±0.009	77.21	1570.93
163.76±0.021	0.743±0.118	0.044±0.02	4.60	34.21
165.374±0.003	0.647±0.221	0.005±0.005	8.32	49.58
166.593±0.005	1.628±0.335	0.01±0.005	39.09	376.12
167.114±0.007	1.591±0.243	0.019±0.007	26.45	307.34
167.782±0.007	2.33±0.318	0.023±0.008	51.18	725.04
168.212±0.005	2.058±0.376	0.012±0.005	56.81	539.12
169.392±0.006	0.868±0.192	0.01±0.006	10.70	87.06
170.086±0.005	0.643±0.184	0.006±0.005	8.34	45.15
172.463±0.013	2.18±0.204	0.056±0.015	25.52	544.96
173.985±0.012	3.397±0.294	0.057±0.012	74.70	1693.49
176.95±0.006	0.672±0.166	0.011±0.011	4.38	43.67
179.236±0.005	0.976±0.225	0.008±0.005	121.27	121.27
180.348±0.009	1.98±0.256	0.028±0.01	32.63	337.11
180.681±0.015	1.824±0.182	0.057±0.016	15.76	275.55
181.707±0.007	1.108±0.203	0.014±0.007	15.46	143.52
182.351±0.005	0.77±0.186	0.008±0.005	10.31	68.05
184.819±0.005	0.79±0.198	0.007±0.005	11.71	60.07
185.073±0.008	0.505±0.159	0.009±0.009	4.50	8.32
185.331±0.026	0.946±0.178	0.054±0.031	4.41	17.23
185.594±0.013	2.179±0.211	0.056±0.017	30.68	449.61
187.121±0.016	2.411±0.19	0.079±0.017	29.49	711.35
190.16±0.016	0.736±0.124	0.033±0.018	4.69	37.66
192.104±0.008	0.572±0.136	0.012±0.007	4.79	24.79
192.705±0.015	0.702±0.126	0.032±0.017	4.23	29.33
193.961±0.033	1.716±0.122	0.162±0.032	11.57	248.72
195.675±0.012	0.6±0.126	0.02±0.013	3.98	22.66
198.528±0.013	0.378±0.157	0.012±0.018	1.97	0.74
198.819±0.021	1.098±0.135	0.063±0.023	6.27	76.01
199.204±0.024	0.971±0.135	0.064±0.028	4.76	46.78
200.449±0.048	1.528±0.118	0.226±0.051	6.43	147.40
207.029±0.053	1.218±0.113	0.192±0.048	5.93	81.13
212.401±0.094	1.105±0.139	0.346±0.142	1.36	38.89
220.743±0.014	0.591±0.125	0.03±0.023	2.52	19.90

Table B9. Resolved oscillations for KIC 7619745 .

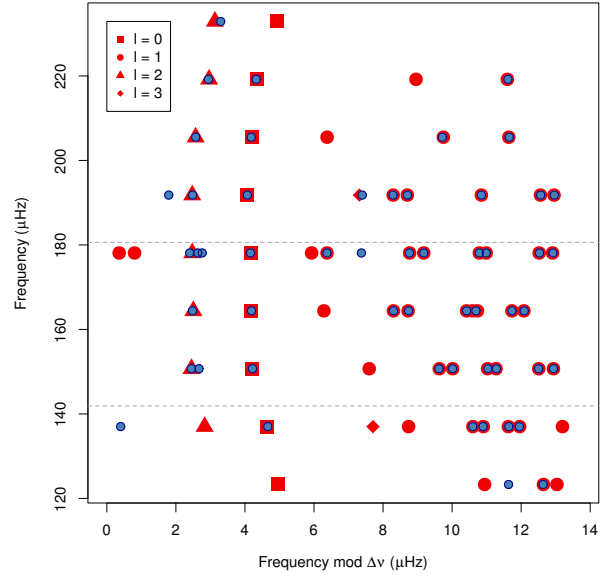
ν_k	H_k	AIC
141.996±0.002	24.341±17.567	21.78
152.631±0.002	21.4±16.24	16.53
156.725±0.001	47.87±30.048	106.10
162.619±0.001	46.85±31.866	90.53
164.669±0.001	85.663±60.049	129.06
171.562±0.001	37.569±29.887	45.63
172.092±0.002	384.319±190.437	105.06
174.598±0.002	26.466±28.051	21.70
178.569±0.002	151.005±59.669	143.22
184.091±0.002	23.311±19.106	23.50
186.726±0.002	58.27±48.794	32.50

Table B10. Unresolved oscillations for KIC 7619745 .**Figure B5.** Same as Fig. 14 for KIC 7619745.

ν_k	A_k	γ_k	SNR	AIC
134.935±0.006	0.463±0.135	0.008±0.009	3.21	14.93
135.937±0.01	0.489±0.126	0.014±0.012	3.00	14.83
137.402±0.006	0.322±0.153	0.006±0.009	1.85	3.93
141.663±0.024	0.87±0.115	0.062±0.023	4.92	50.75
147.599±0.01	0.611±0.134	0.018±0.014	3.92	26.44
147.898±0.01	0.739±0.134	0.021±0.011	5.59	46.42
148.643±0.03	0.455±0.121	0.038±0.029	1.68	3.71
148.948±0.009	0.526±0.13	0.015±0.012	3.35	17.65
153.149±0.017	0.984±0.128	0.048±0.018	5.90	76.21
153.37±0.014	0.442±0.142	0.018±0.019	2.27	3.20
154.917±0.021	1.65±0.138	0.092±0.022	13.54	276.48
160.32±0.004	0.752±0.206	0.006±0.005	10.21	69.15
161.737±0.013	1.054±0.153	0.033±0.013	7.55	80.60
161.983±0.013	1.198±0.158	0.036±0.013	9.23	121.53
163.636±0.008	0.507±0.133	0.01±0.006	4.52	18.82
166.88±0.03	1.683±0.126	0.137±0.028	12.09	243.53
168.59±0.015	2.138±0.181	0.07±0.016	25.69	551.54
172.703±0.006	0.435±0.152	0.006±0.006	3.96	13.05
173.14±0.007	0.583±0.145	0.01±0.006	5.52	30.48
174.82±0.008	1.436±0.221	0.02±0.008	20.95	193.31
175.091±0.017	1.284±0.153	0.048±0.016	8.34	130.37
176.135±0.007	1.667±0.257	0.018±0.008		372.31
180.5±0.013	1.923±0.193	0.05±0.014	22.95	420.94
180.863±0.008	1.092±0.19	0.019±0.01	12.39	85.05
182.258±0.012	2.745±0.242	0.057±0.013	46.96	1056.25
185.473±0.039	0.698±0.116	0.079±0.036	3.43	18.36
186.865±0.004	0.865±0.265	0.006±0.004	12.88	89.62
187.28±0.005	0.966±0.216	0.009±0.005	14.79	118.80
188.888±0.007	2.238±0.343	0.019±0.008	52.88	287.39
189.087±0.015	1.892±0.205	0.052±0.016	18.89	212.10
190.631±0.012	0.973±0.141	0.031±0.012	8.11	85.22
191.02±0.004	0.929±0.249	0.006±0.004	15.35	103.04
194.284±0.019	2.607±0.182	0.104±0.02	30.43	768.75
195.871±0.015	2.936±0.221	0.082±0.016	45.09	1077.82
199.198±0.06	0.624±0.119	0.092±0.043	2.45	9.06
200.506±0.005	0.818±0.196	0.008±0.005	11.61	80.58
202.65±0.017	2.466±0.187	0.084±0.016	31.97	774.14
204.365±0.013	0.745±0.129	0.026±0.012	5.49	40.05
204.761±0.005	0.928±0.215	0.009±0.006	13.13	100.55
208.074±0.048	1.476±0.119	0.217±0.051	6.17	129.57
209.681±0.026	1.731±0.133	0.13±0.03	12.03	258.60
215.218±0.06	1.033±0.112	0.156±0.042	5.21	50.70
217.155±0.033	1.375±0.118	0.136±0.033	8.77	138.78
222.143±0.062	0.966±0.139	0.183±0.093	2.41	34.72
223.525±0.095	0.933±0.139	0.269±0.12	1.99	22.39
230.819±0.058	0.784±0.129	0.147±0.075	2.88	19.16
236.197±0.174	0.875±0.164	0.4±0.209	1.49	11.45

Table B11. Resolved oscillations for KIC 8366239 .

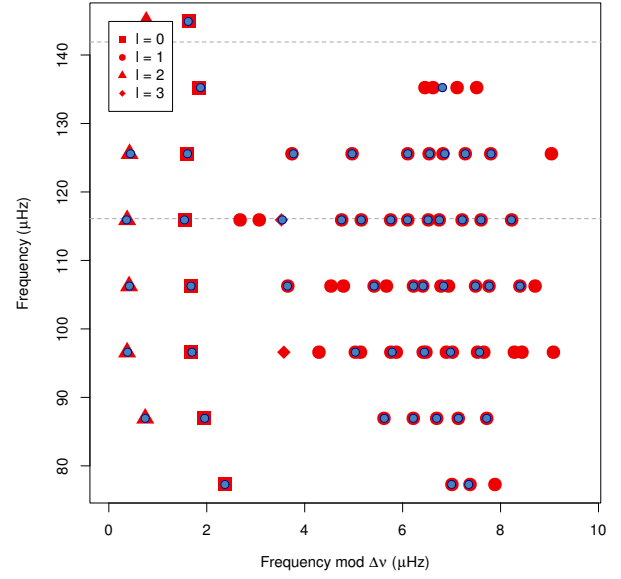
ν_k	H_k	AIC
160.716±0.001	73.978±66.04	64.27
163.206±0.002	32.866±20.642	41.90
176.489±0.001	557.175±275.38	240.20
180.734±0.002	21.878±24.397	6.87
184.476±0.001	55.231±34.098	89.87
193.592±0.002	22.057±14.502	15.85
200.089±0.002	47.01±32.87	52.35

Table B12. Unresolved oscillations for KIC 8366239 .**Figure B6.** Same as Fig. 14 for KIC 8366239.

ν_k	A_k	γ_k	SNR	AIC
79.651±0.014	0.714±0.122	0.032±0.017	5.01	36.86
84.28±0.034	0.547±0.114	0.051±0.028	2.45	8.76
84.631±0.01	0.641±0.153	0.014±0.014	4.60	33.92
87.684±0.053	0.708±0.137	0.101±0.068	2.89	16.09
88.897±0.05	0.968±0.113	0.138±0.042	4.14	44.92
92.566±0.004	0.457±0.18	0.005±0.007	3.98	15.80
93.159±0.006	0.631±0.152	0.01±0.008	5.66	36.76
93.635±0.007	1.06±0.186	0.016±0.007	13.59	137.58
94.078±0.007	0.718±0.163	0.011±0.007	7.03	51.87
94.657±0.008	0.492±0.137	0.008±0.006	4.57	19.14
96.982±0.022	1.258±0.126	0.079±0.023	8.62	134.50
98.298±0.018	1.307±0.135	0.066±0.021	9.82	157.92
101.635±0.004	0.505±0.175	0.005±0.008	4.14	27.70
102.385±0.02	0.967±0.136	0.038±0.016	8.45	73.80
103.044±0.008	1.755±0.242	0.024±0.008	29.08	359.87
103.578±0.01	1.808±0.217	0.033±0.01	27.26	360.03
104.171±0.018	1.292±0.142	0.055±0.017	11.77	139.14
106.68±0.022	2.128±0.153	0.119±0.025	19.99	436.63
107.938±0.009	3.341±0.343	0.04±0.01	87.72	1577.71
109.909±0.005	0.85±0.2	0.009±0.006	11.52	82.25
113.097±0.018	2.527±0.193	0.093±0.022	44.53	698.26
116.282±0.018	2.582±0.188	0.098±0.021	31.98	702.40
117.465±0.014	2.889±0.232	0.071±0.016	47.14	980.34
119.462±0.023	0.915±0.124	0.067±0.029	5.17	49.87
121.075±0.004	0.764±0.272	0.005±0.005	10.17	62.83
122.019±0.009	1.233±0.19	0.022±0.009	15.77	140.77
122.439±0.011	1.622±0.211	0.033±0.012	17.88	176.17
122.671±0.009	2.008±0.275	0.024±0.009	35.10	347.20
123.139±0.007	0.873±0.178	0.012±0.006	10.70	67.97
123.521±0.006	0.612±0.168	0.007±0.006	6.51	34.59
124.141±0.012	0.609±0.129	0.018±0.011	4.27	23.28
126.023±0.029	1.952±0.137	0.158±0.034	13.10	321.32
127.186±0.018	1.935±0.161	0.084±0.02	19.18	357.16
129.35±0.029	0.664±0.125	0.057±0.034	3.16	18.07
131.684±0.013	0.637±0.127	0.022±0.012	4.66	23.24
132.132±0.02	1.052±0.134	0.058±0.022	5.61	73.44
132.44±0.019	0.849±0.134	0.045±0.021	4.46	36.15
132.86±0.015	0.737±0.14	0.025±0.017	5.15	36.54
133.384±0.013	0.602±0.131	0.02±0.015	4.15	22.16
135.925±0.065	1.49±0.126	0.3±0.077	3.92	106.93
137.113±0.036	1.346±0.128	0.155±0.049	6.25	103.34
142.053±0.146	1.209±0.129	0.477±0.135	3.67	41.11
146.521±0.15	1.195±0.14	0.5±0.17	3.45	37.98

Table B13. Resolved oscillations for KIC 8475025 .

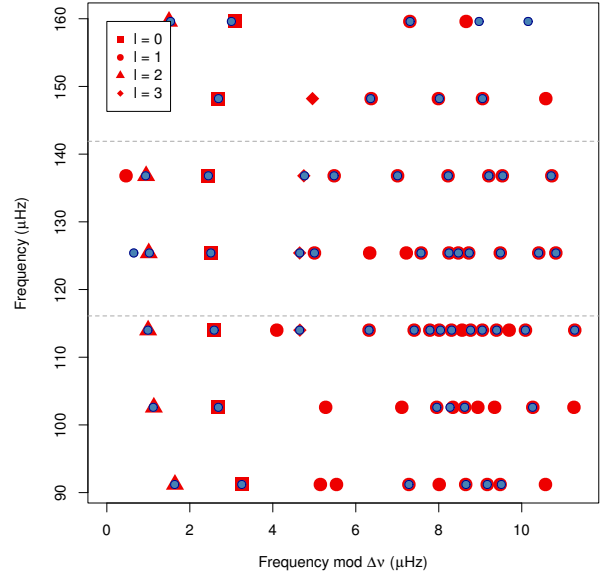
ν_k	H_k	AIC
111.677±0.001	260.158±122.581	289.05
112.48±0.001	664.33±239.881	370.03
112.677±0	4016.409±2042.859	238.18
113.747±0.001	127.029±72.124	124.57
114.027±0.001	62.034±28.206	105.55
114.658±0.001	55.77±36.614	62.15
120.674±0.001	49.183±25.796	83.53
121.679±0.001	58.492±31.924	83.11
130.547±0.002	33.018±19.354	45.65

Table B14. Unresolved oscillations for KIC 8475025 .**Figure B7.** Same as Fig. 14 for KIC 8475025.

ν_k	A_k	γ_k	SNR	AIC
92.835±0.023	0.538±0.148	0.038±0.044	2.41	11.07
94.452±0.014	0.737±0.123	0.03±0.015	4.82	41.77
98.481±0.004	0.462±0.175	0.005±0.008	2.86	19.09
99.855±0.008	0.625±0.152	0.012±0.012	4.68	33.27
100.369±0.036	0.682±0.131	0.081±0.051	1.75	16.37
100.708±0.027	0.462±0.131	0.021±0.02	2.82	6.70
103.718±0.029	0.942±0.114	0.081±0.027	5.08	56.33
105.288±0.01	1.42±0.177	0.032±0.01	16.49	247.33
110.552±0.006	1.159±0.229	0.012±0.006	18.69	177.09
110.872±0.008	0.419±0.139	0.009±0.012	2.44	6.67
111.224±0.014	1±0.138	0.04±0.019	8.12	89.73
112.861±0.004	0.553±0.184	0.006±0.006	5.43	27.77
114.99±0.02	1.372±0.134	0.077±0.024	10.04	169.46
116.587±0.012	2.311±0.217	0.052±0.013	36.78	722.02
118.647±0.006	0.654±0.163	0.009±0.006	6.53	42.67
122.041±0.017	0.563±0.149	0.025±0.02	3.15	6.15
122.311±0.008	2.162±0.275	0.027±0.009	46.36	634.53
122.767±0.01	0.533±0.144	0.012±0.009	4.60	11.74
123.048±0.005	1.919±0.362	0.011±0.005	48.37	523.84
123.395±0.008	0.526±0.139	0.01±0.008	4.49	16.32
124.087±0.003	1.299±0.353	0.005±0.003		316.31
126.049±0.003	1.008±0.323	0.005±0.004	78.82	79.69
126.424±0.009	2.879±0.31	0.037±0.011	3.69	1160.88
127.907±0.009	3.588±0.375	0.038±0.01	102.42	1977.79
130.049±0.013	0.947±0.135	0.034±0.014	7.22	77.59
132.971±0.006	1.784±0.294	0.016±0.007	40.39	410.19
133.647±0.006	0.911±0.258	0.007±0.007	14.15	25.10
133.873±0.008	3.305±0.399	0.029±0.009	97.30	1468.03
134.134±0.015	0.867±0.189	0.02±0.011	7.31	18.32
134.886±0.006	1.425±0.267	0.012±0.006	25.52	252.12
135.807±0.011	0.373±0.124	0.01±0.009	2.40	3.19
137.736±0.017	2.916±0.206	0.096±0.02	7.61	1037.65
139.247±0.012	3.051±0.265	0.058±0.013	45.98	1213.00
141.564±0.008	0.648±0.143	0.013±0.009	57.61	35.23
142.277±0.004	0.419±0.152	0.005±0.006	5.62	14.95
143.807±0.004	1.269±0.3	0.006±0.003	4.31	243.06
145.03±0.014	1.843±0.172	0.06±0.015		393.89
146.008±0.011	1.343±0.171	0.033±0.012	20.43	188.43
146.343±0.019	0.494±0.129	0.024±0.018	14.68	6.11
147.51±0.008	0.686±0.141	0.015±0.009	2.37	39.37
149.434±0.032	1.67±0.127	0.159±0.036	10.36	212.46
150.891±0.027	1.775±0.133	0.137±0.031	12.61	268.41
154.558±0.007	0.486±0.131	0.01±0.008	3.58	15.80
156.214±0.033	0.82±0.127	0.069±0.038	4.40	36.58
157.254±0.026	1.035±0.119	0.085±0.029	6.06	72.42
161.135±0.067	1.086±0.123	0.212±0.069	3.40	46.86
162.602±0.056	1.294±0.117	0.221±0.057	4.81	86.58
166.909±0.014	0.484±0.121	0.023±0.019	2.23	9.81
168.573±0.052	0.459±0.118	0.058±0.036	1.43	1.91
169.754±0.013	0.46±0.119	0.019±0.015	2.75	9.20

Table B15. Resolved oscillations for KIC 8718745 .

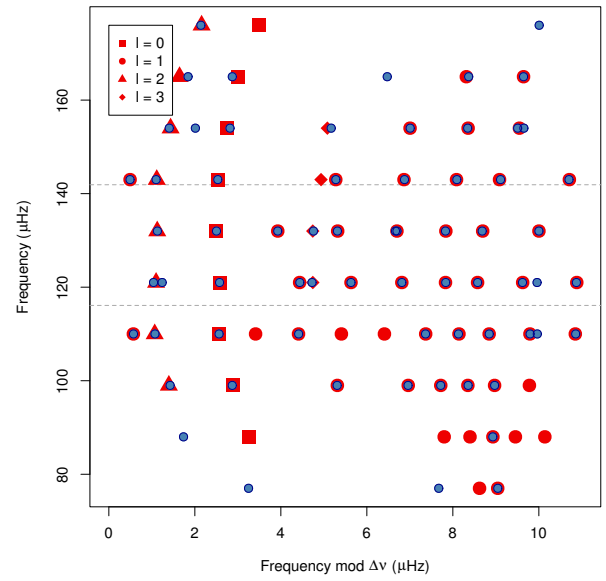
ν_k	H_k	AIC
120.32±0.001	160.198±104.719	269.02
121.407±0.001	245.653±96.669	215.21
121.788±0.001	41.844±34.991	31.42
125.275±0.001	195.449±106.007	174.84
130.403±0.001	31.414±25.306	48.84
136.222±0.001	189.148±112.914	313.72

Table B16. Unresolved oscillations for KIC 8718745 .**Figure B8.** Same as Fig. 14 for KIC 8718745.

ν_k	A_k	γ_k	SNR	AIC
80.249±0.008	0.378±0.121	0.008±0.006	2.21	6.98
86.045±0.014	0.469±0.116	0.02±0.015	2.76	9.61
89.737±0.035	0.844±0.12	0.091±0.042	3.91	36.92
96.93±0.006	0.652±0.151	0.01±0.007	6.42	42.99
100.425±0.045	0.936±0.116	0.125±0.045	4.26	42.55
101.87±0.019	1.094±0.125	0.059±0.018	7.94	101.51
105.958±0.004	0.434±0.13	0.005±0.006	2.81	31.92
106.718±0.009	0.636±0.133	0.016±0.009	4.86	32.63
107.355±0.008	1.174±0.176	0.023±0.01	14.35	165.82
107.972±0.006	0.656±0.166	0.009±0.006	7.11	43.39
110.573±0.004	0.452±0.163	0.005±0.006	2.14	16.80
111.074±0.016	1.131±0.138	0.053±0.023	8.90	114.17
112.564±0.013	1.798±0.174	0.054±0.014	20.76	393.35
117.365±0.004	1.176±0.274	0.007±0.004		201.51
118.131±0.01	1.713±0.197	0.036±0.011	23.38	367.12
118.846±0.005	1.852±0.357	0.011±0.005	47.35	500.82
119.796±0.009	0.504±0.13	0.012±0.008	3.91	14.44
119.964±0.022	0.462±0.136	0.029±0.03	1.80	4.82
120.857±0.008	0.404±0.127	0.008±0.008	3.00	7.18
122.039±0.009	1.583±0.239	0.023±0.01	24.24	147.43
122.24±0.027	1.26±0.167	0.085±0.037	4.64	64.29
123.575±0.012	2.934±0.263	0.055±0.013	57.46	1203.87
125.726±0.033	0.995±0.123	0.106±0.042	7.06	53.32
128.834±0.007	2.622±0.379	0.02±0.007	83.50	958.20
129.577±0.007	2.763±0.372	0.023±0.008	87.19	1069.88
130.959±0.016	0.492±0.122	0.022±0.015	2.77	7.59
133.129±0.02	3.172±0.197	0.13±0.023	41.54	1132.88
134.503±0.012	3.432±0.3	0.057±0.013	79.44	1434.37
136.758±0.013	1.064±0.143	0.04±0.018	8.46	96.99
138.701±0.004	1.577±0.376	0.008±0.005		344.67
139.829±0.008	2.773±0.349	0.026±0.008	69.31	1101.82
140.683±0.01	1.876±0.215	0.036±0.011	27.21	408.43
142.002±0.007	1.071±0.2	0.014±0.007	14.90	126.07
144.1±0.023	2.525±0.166	0.134±0.025	24.25	590.62
145.534±0.019	3.167±0.205	0.117±0.021	43.98	1139.07
149.876±0.008	0.849±0.17	0.014±0.008	9.24	73.38
151.093±0.012	2.052±0.208	0.046±0.012	29.38	527.01
152.11±0.019	1.25±0.135	0.063±0.021	9.70	128.98
153.702±0.006	0.846±0.193	0.009±0.005	11.18	78.12
155.405±0.03	1.744±0.135	0.14±0.032	10.90	225.32
156.012±0.018	0.574±0.149	0.024±0.017	4.47	5.29
156.818±0.044	1.886±0.127	0.247±0.051	7.96	241.66
159.171±0.07	0.695±0.127	0.127±0.06	2.62	10.48
161.008±0.011	0.767±0.141	0.02±0.012	6.74	49.35
162.345±0.022	1.526±0.133	0.092±0.022	11.77	213.28
163.507±0.007	0.579±0.16	0.01±0.011	4.22	19.23
163.652±0.019	0.636±0.14	0.039±0.03	2.74	16.61
166.843±0.793	1.249±0.483	0.4±0.785	2.48	38.17
167.871±0.138	1.329±0.154	0.4±0.14	3.13	49.01
173.368±0.057	1.025±0.118	0.177±0.057	4.29	45.29
174.644±0.037	0.878±0.117	0.087±0.033	4.41	39.50
178.141±0.145	0.872±0.309	0.4±0.537	1.48	11.08
186.008±0.02	0.471±0.129	0.033±0.033	1.87	6.09

Table B17. Resolved oscillations for KIC 9145955 .

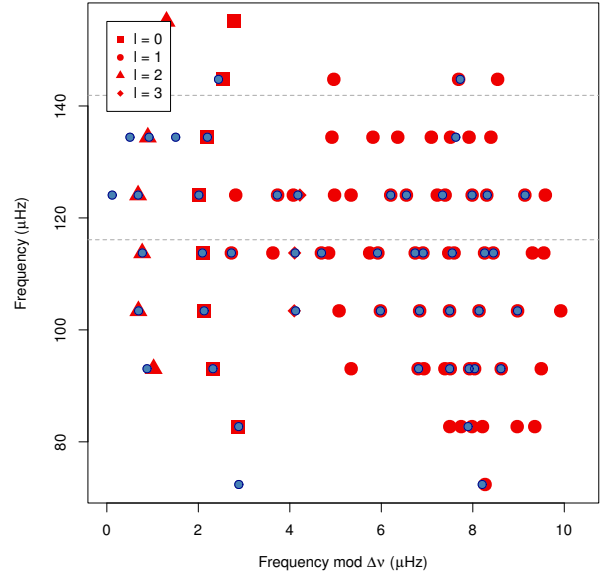
ν_k	H_k	AIC
125.441±0.002	65.9±72.12	77.12
126.631±0.002	45.974±28.761	52.20
127.814±0.001	93.732±53.151	88.95
130.619±0.001	269.053±177.911	281.88
131.873±0.002	75.77±52.634	39.76
135.928±0.002	39.794±29.304	36.37
137.316±0.002	33.339±19.358	41.32
143.493±0.002	22.378±16.455	14.78
148.279±0.001	86.423±69.777	122.20

Table B18. Unresolved oscillations for KIC 9145955 .**Figure B9.** Same as Fig. 14 for KIC 9145955.

ν_k	A_k	γ_k	SNR	AIC
75.265±0.026	0.445±0.11	0.03±0.018	2.27	4.80
80.586±0.02	0.542±0.121	0.032±0.024	2.77	13.09
85.603±0.042	0.53±0.113	0.053±0.028	2.32	7.40
90.617±0.082	0.975±0.123	0.22±0.08	3.56	33.87
93.939±0.06	0.771±0.117	0.124±0.049	3.17	19.98
95.38±0.015	1.248±0.141	0.05±0.017	10.37	155.80
99.875±0.007	0.781±0.157	0.015±0.01	7.88	59.94
100.554±0.018	1.061±0.131	0.051±0.02	7.38	96.20
100.979±0.006	0.701±0.166	0.01±0.007	7.39	39.51
101.101±0.006	0.673±0.161	0.01±0.007	6.77	36.06
104.094±0.02	1.704±0.144	0.087±0.02	15.31	288.58
105.527±0.014	2.112±0.184	0.066±0.016	25.84	539.32
107.527±0.042	0.63±0.118	0.07±0.035	2.83	12.68
110.234±0.004	1.213±0.312	0.006±0.004	26.68	211.47
110.895±0.003	3.016±0.807	0.005±0.003	145.69	1424.03
111.538±0.009	1.467±0.195	0.027±0.009	19.46	255.73
112.377±0.011	0.609±0.133	0.018±0.013	4.62	24.01
114.516±0.015	2.628±0.208	0.077±0.017	37.71	823.90
115.829±0.009	3.682±0.388	0.039±0.01	121.35	1935.49
116.463±0.003	0.647±0.174	0.005±0.004	6.05	50.66
117.856±0.015	0.942±0.13	0.04±0.016	7.14	69.69
119.657±0.009	0.61±0.139	0.014±0.009	5.30	26.73
120.477±0.006	1.707±0.299	0.014±0.006	35.32	295.94
120.655±0.006	1.205±0.251	0.011±0.006	19.29	98.81
121.29±0.01	3.095±0.307	0.044±0.011	65.65	1339.27
121.998±0.003	1.541±0.376	0.005±0.003	33.60	413.12
124.764±0.02	2.937±0.189	0.124±0.023	34.95	947.38
126.092±0.011	3.342±0.302	0.053±0.012	78.28	1385.98
128.256±0.038	0.96±0.12	0.109±0.039	3.83	43.94
130.285±0.003	0.951±0.267	0.005±0.004	23.56	142.43
130.629±0.01	1.019±0.164	0.022±0.009	11.21	85.38
131.419±0.019	2.117±0.163	0.094±0.02	20.33	479.64
132.064±0.012	0.964±0.155	0.026±0.012	9.19	61.18
132.396±0.01	0.668±0.142	0.016±0.009	5.94	28.03
133.223±0.007	0.455±0.145	0.006±0.005	4.17	15.87
134.926±0.046	0.6±0.154	0.051±0.037	2.58	5.60
135.343±0.021	1.498±0.143	0.084±0.025	10.39	174.02
135.925±0.006	0.484±0.178	0.007±0.008	4.29	8.71
136.618±0.024	2.089±0.145	0.133±0.028	16.61	423.06
142.048±0.081	1.779±0.121	0.4±0.073	7.16	165.47
145.92±0.042	1.206±0.125	0.161±0.052	5.02	76.05
147.201±0.058	1.204±0.121	0.211±0.06	4.48	66.55
152.485±0.085	1.158±0.129	0.312±0.108	3.69	49.57

Table B19. Resolved oscillations for KIC 9267654 .

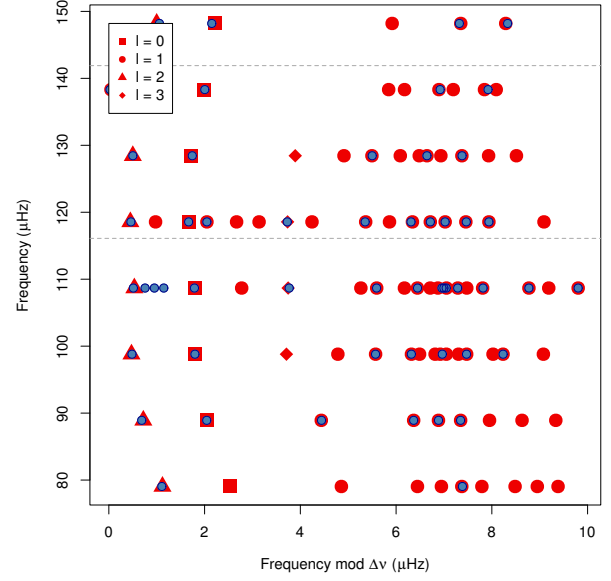
ν_k	H_k	AIC
101.675±0.002	27.707±16.198	38.89
109.379±0.001	51.324±38.263	60.76
118.433±0.001	32.598±26.992	43.16
122.191±0.001	148.856±62.82	216.54
124.198±0.002	33.064±25.49	20.94
127.806±0.002	28.69±19.506	23.18

Table B20. Unresolved oscillations for KIC 9267654 .**Figure B10.** Same as Fig. 14 for KIC 9267654.

ν_k	A_k	γ_k	SNR	AIC
80.147±0.016	0.414±0.114	0.021±0.017	1.77	4.89
86.425±0.017	0.875±0.127	0.049±0.026	5.66	57.64
89.607±0.008	0.572±0.145	0.015±0.017	3.57	25.78
90.965±0.018	1.099±0.126	0.056±0.017	8.24	106.28
93.362±0.016	0.374±0.109	0.01±0.014	3.38	6.99
95.806±0.023	0.958±0.124	0.068±0.028	4.51	60.84
96.267±0.006	0.979±0.201	0.01±0.005	13.95	110.74
99.283±0.016	1.486±0.147	0.063±0.018	13.42	225.33
100.599±0.01	2.131±0.228	0.04±0.011	33.68	613.94
105.119±0.003	0.954±0.293	0.005±0.005		92.12
105.765±0.055	1.881±0.2	0.106±0.079	21.10	350.51
106.271±0.006	1.543±0.26	0.015±0.007		227.44
109.192±0.01	2.411±0.249	0.041±0.012	62.90	748.24
109.828±0.008	0.423±0.17	0.006±0.008	3.68	3.36
110.468±0.011	2.742±0.274	0.046±0.012	54.78	1031.02
112.447±0.018	1.037±0.13	0.049±0.017	7.98	82.80
114.273±0.005	0.815±0.237	0.006±0.004	12.51	59.34
115.128±0.005	2.089±0.49	0.009±0.005	51.27	216.39
115.679±0.037	2.605±0.165	0.217±0.039	47.31	327.53
115.727±0.036	1.754±2.99	0.006±0.038		17.65
119.021±0.017	3.194±0.224	0.096±0.018	79.50	1121.02
120.227±0.012	3.549±0.313	0.058±0.013		1494.60
122.287±0.03	0.867±0.136	0.061±0.036	15.30	40.87
123.914±0.005	1.007±0.261	0.007±0.004	3.31	104.12
124.872±0.017	1.701±0.169	0.062±0.023	21.74	265.56
125.276±0.008	0.814±0.187	0.013±0.008	9.79	23.92
125.584±0.011	2.388±0.241	0.046±0.013	38.63	648.03
126.026±0.012	0.541±0.187	0.007±0.027	4.37	11.62
128.942±0.026	2.241±0.152	0.144±0.03	18.22	450.64
130.183±0.018	2.38±0.18	0.093±0.02	27.57	582.28
133.941±0.004	0.648±0.204	0.005±0.005	7.76	45.39
135.084±0.021	1.729±0.145	0.099±0.026	13.36	272.67
135.818±0.018	1.182±0.142	0.06±0.024	8.56	97.52
138.345±0.043	0.472±0.159	0.041±0.048	2.37	1.27
139.191±0.044	1.676±0.124	0.223±0.049	7.11	182.31
140.324±0.03	1.286±0.129	0.114±0.035	7.03	100.67
145.24±0.053	1.018±0.118	0.157±0.05	3.87	45.18
146.241±0.043	0.951±0.119	0.111±0.039	4.57	42.22
149.256±0.083	1.261±0.138	0.322±0.116	2.97	56.21
150.35±0.096	1.016±0.157	0.289±0.152	1.89	24.71
155.522±0.062	0.803±0.158	0.157±0.119	2.26	20.35
156.53±0.017	0.4±0.122	0.023±0.023	1.67	2.72
163.808±0.011	0.325±0.148	0.005±0.032	1.57	3.68

Table B21. Resolved oscillations for KIC 9475697 .

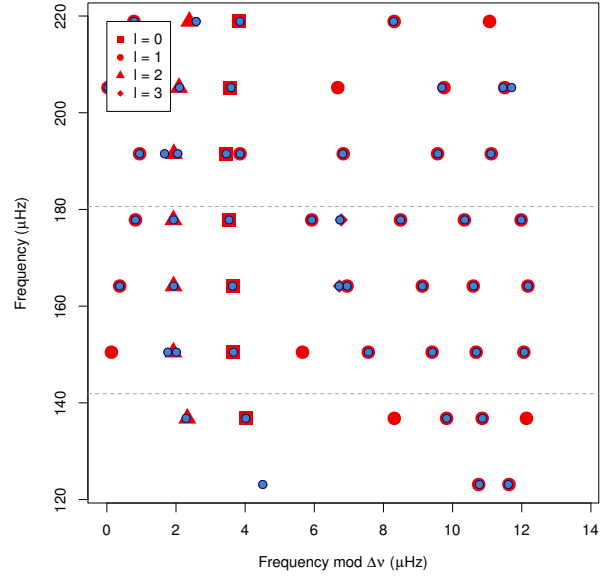
ν_k	H_k	AIC
95.287±0.001	160.059±74.849	102.65
104.371±0.001	51.343±52.416	80.67
107.036±0.001	104.647±63.325	106.75
109.437±0.002	124.327±67.948	49.69
109.631±0.002	35.095±33.639	29.75
115.967±0.002	98.762±73.906	28.14
116.496±0.002	189.291±93.649	111.97
117.454±0.001	96.18±78.639	100.17
118.483±0.002	44.193±44.658	21.69
120.608±0.002	40.833±39.158	18.28
126.499±0.002	132.886±65.345	137.01

Table B22. Unresolved oscillations for KIC 9475697 .**Figure B11.** Same as Fig. 14 for KIC 9475697.

ν_k	A_k	γ_k	SNR	AIC
127.629±0.042	0.649±0.116	0.075±0.038	3.07	15.11
133.897±0.01	0.569±0.129	0.017±0.013	3.87	23.28
134.732±0.007	0.549±0.135	0.011±0.007	4.52	25.07
139.092±0.049	0.635±0.13	0.098±0.063	1.90	10.41
140.819±0.012	0.831±0.132	0.027±0.012	6.63	62.75
146.627±0.005	1.1±0.236	0.01±0.005	17.92	167.18
147.663±0.014	0.937±0.132	0.034±0.013	7.41	81.72
152.245±0.014	0.583±0.126	0.02±0.012	4.22	17.65
152.49±0.028	0.714±0.119	0.058±0.028	2.13	23.47
154.142±0.019	1.496±0.137	0.075±0.018	12.86	227.25
158.046±0.005	0.397±0.144	0.005±0.007	3.71	11.86
159.894±0.012	0.576±0.122	0.017±0.009	4.89	23.50
161.165±0.014	1.256±0.144	0.045±0.014	11.49	166.28
162.554±0.007	0.76±0.165	0.011±0.006	8.53	63.44
166.097±0.014	1.354±0.148	0.05±0.017	13.12	191.51
167.795±0.015	1.813±0.164	0.064±0.016	19.57	388.16
170.879±0.026	0.522±0.111	0.03±0.015	2.63	11.04
174.765±0.01	2.214±0.237	0.039±0.01	35.07	696.65
176.344±0.004	1.174±0.276	0.007±0.004	23.99	203.08
178.665±0.006	0.726±0.177	0.008±0.005	8.65	55.14
179.77±0.017	1.965±0.162	0.08±0.018	20.02	422.53
181.375±0.011	3.091±0.292	0.048±0.011	62.62	1409.38
184.583±0.005	0.367±0.143	0.005±0.008	1.68	6.43
186.339±0.006	0.653±0.165	0.008±0.005	7.58	45.51
188.191±0.014	1.826±0.173	0.057±0.015	20.66	406.66
189.824±0.006	1.304±0.24	0.013±0.006	21.41	232.91
193.189±0.009	1.051±0.173	0.021±0.01	11.40	93.51
193.572±0.016	1.395±0.147	0.058±0.018	11.35	177.29
194.975±0.021	1.814±0.143	0.1±0.023	15.05	335.00
198.346±0.023	0.719±0.117	0.05±0.025	3.57	28.76
201.091±0.009	1.551±0.205	0.027±0.009	21.39	311.80
202.627±0.018	1.613±0.146	0.071±0.017	14.92	278.28
207.301±0.037	1.153±0.121	0.14±0.047	5.02	76.47
208.792±0.041	1.35±0.118	0.165±0.042	6.97	118.54
214.892±0.008	0.456±0.141	0.012±0.016	2.86	12.01
216.659±0.021	0.815±0.119	0.054±0.024	3.65	42.71
216.906±0.018	0.384±0.139	0.012±0.015	2.25	2.75
219.666±0.005	0.389±0.141	0.005±0.005	3.44	11.26
221.464±0.176	0.799±0.141	0.309±0.137	1.32	9.78
222.731±0.045	0.529±0.127	0.065±0.046	2.02	5.08
227.174±0.019	0.525±0.115	0.032±0.02	2.12	11.41

Table B23. Resolved oscillations for KIC 9882316 .

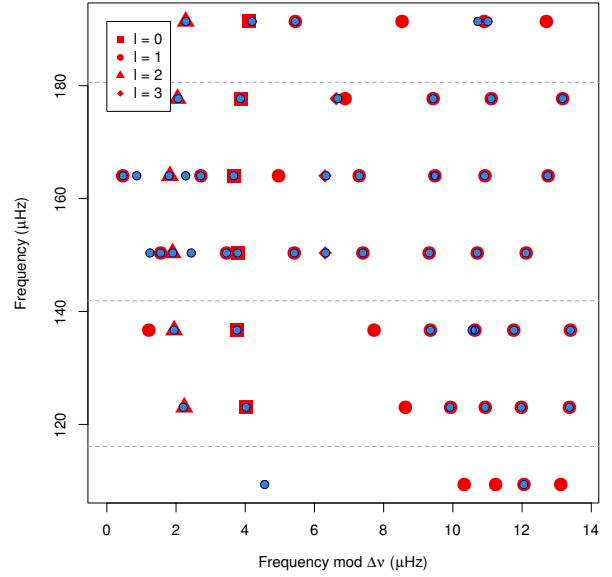
ν_k	H_k	AIC
164.53±0.002	58.253±29.131	89.35
171.109±0.001	74.191±36.357	134.04
173.286±0.001	117.735±61.44	167.85
183.765±0.001	116.229±114.666	195.50
192.468±0.002	59.061±28.749	73.36
195.372±0.002	41.477±32.269	28.23
205.232±0.002	35.658±19.119	50.39

Table B24. Unresolved oscillations for KIC 9882316 .**Figure B12.** Same as Fig. 14 for KIC 9882316.

ν_k	A_k	γ_k	SNR	AIC
113.921±0.019	0.594±0.113	0.032±0.016	3.43	19.40
121.413±0.005	0.723±0.174	0.008±0.005	8.84	62.91
125.239±0.022	0.688±0.115	0.047±0.023	3.50	25.83
127.056±0.045	0.818±0.111	0.103±0.036	3.74	30.19
132.948±0.014	0.516±0.115	0.02±0.011	3.63	14.52
133.965±0.007	1.378±0.214	0.019±0.007	19.63	257.34
135.009±0.005	0.758±0.183	0.008±0.005	9.38	68.89
136.397±0.005	0.379±0.13	0.005±0.005	4.05	14.93
138.644±0.013	1.426±0.158	0.045±0.014	13.96	226.23
140.465±0.015	1.881±0.169	0.064±0.015	21.01	427.05
146.052±0.004	1.323±0.333	0.007±0.004	27.18	260.51
147.338±0.003	2.77±0.891	0.005±0.004		215.25
148.466±0.004	1.448±0.318	0.008±0.004	32.82	322.95
151.922±0.005	0.699±0.201	0.005±0.004	10.27	41.04
152.277±0.007	2.816±0.396	0.021±0.007	84.70	1233.10
152.809±0.006	0.633±0.183	0.009±0.012	5.18	28.71
154.147±0.01	3.134±0.307	0.045±0.011	74.87	1470.39
156.689±0.009	1.097±0.163	0.025±0.011	10.91	132.35
159.691±0.007	1.648±0.255	0.018±0.007	29.23	370.15
161.073±0.006	4.062±0.584	0.019±0.006	162.48	2829.68
162.483±0.006	1.531±0.267	0.014±0.006	29.11	321.66
164.509±0.011	0.622±0.131	0.017±0.01	4.83	27.39
164.902±0.005	0.795±0.206	0.008±0.007	8.81	65.15
165.84±0.006	3.272±0.473	0.019±0.006	107.71	1592.61
166.318±0.013	1.158±0.159	0.035±0.014	11.42	90.05
166.751±0.009	0.637±0.154	0.015±0.013	4.96	20.53
167.709±0.009	4.151±0.428	0.038±0.009	126.24	2790.59
170.372±0.016	0.896±0.125	0.042±0.017	5.89	62.40
173.503±0.015	0.858±0.282	0.018±0.019		2.83
173.53±0.004	1.705±0.563	0.005±0.004		83.46
174.955±0.011	2.18±0.225	0.043±0.011	32.87	652.71
179.77±0.021	1.854±0.147	0.098±0.022	15.37	339.41
181.571±0.024	2.168±0.146	0.131±0.024	19.61	487.27
184.384±0.043	0.888±0.116	0.107±0.04	4.78	37.49
187.142±0.011	1.056±0.155	0.025±0.009	11.22	119.31
188.817±0.015	1.591±0.154	0.06±0.016	15.14	282.02
190.883±0.009	0.703±0.139	0.017±0.01	5.65	43.47
193.663±0.045	1.032±0.117	0.139±0.045	4.41	53.93
195.578±0.054	1.321±0.113	0.207±0.048	6.13	100.40
196.825±0.007	0.449±0.13	0.009±0.007	3.75	11.41
202.104±0.039	0.731±0.127	0.088±0.046	1.95	19.30
202.393±0.014	0.662±0.133	0.023±0.014	4.53	25.51

Table B25. Resolved oscillations for KIC 10123207 .

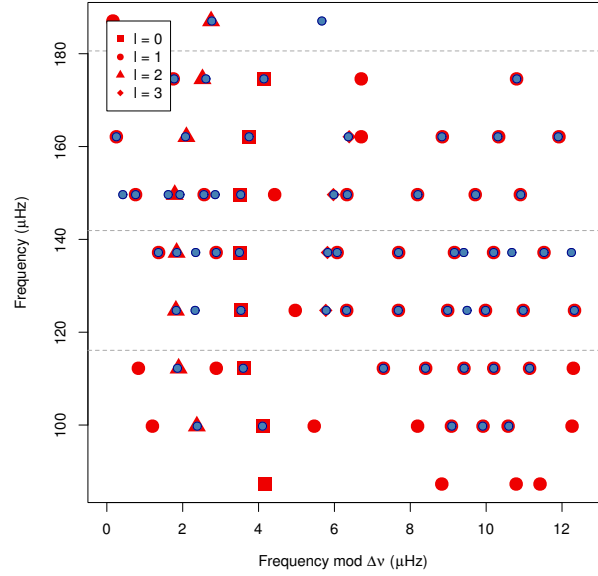
ν_k	H_k	AIC
147.259±0.002	31.897±30.753	1.15
150.097±0.001	68.076±44.97	85.87
151.615±0.002	24.189±16.691	20.79
153.827±0.002	58.123±48.835	28.75
155.787±0.001	204.867±155.299	388.83
157.77±0.001	178.437±102.431	234.49
171.337±0.001	179.599±101.707	218.50
176.783±0.001	269.282±129.638	156.98
179.262±0.002	55.018±31.015	62.97

Table B26. Unresolved oscillations for KIC 10123207 .**Figure B13.** Same as Fig. 14 for KIC 10123207.

ν_k	A_k	γ_k	SNR	AIC
102.143±0.014	0.489±0.12	0.02±0.016	2.75	11.50
103.863±0.038	0.67±0.116	0.079±0.039	2.77	16.41
109.669±0.005	0.521±0.164	0.006±0.007	3.70	23.01
110.356±0.015	0.883±0.125	0.04±0.016	6.34	64.22
114.092±0.06	1.025±0.12	0.188±0.065	3.81	45.00
115.826±0.021	1.193±0.125	0.073±0.022	8.49	119.84
119.522±0.006	0.413±0.13	0.008±0.008	2.93	9.82
120.631±0.006	0.428±0.139	0.005±0.005	3.75	15.46
122.429±0.006	1.625±0.263	0.016±0.006	29.48	386.43
123.376±0.004	0.953±0.247	0.007±0.005	14.57	118.33
126.53±0.012	1.714±0.182	0.046±0.016	23.34	343.85
127.027±0.007	0.661±0.158	0.01±0.006	7.48	31.77
128.236±0.015	2.372±0.195	0.071±0.016	32.32	727.07
130.483±0.013	0.581±0.123	0.019±0.011	4.27	22.13
131.02±0.006	0.626±0.152	0.01±0.007	5.78	36.37
133.685±0.004	1.875±0.439	0.006±0.003		552.96
134.197±0.036	0.562±0.131	0.05±0.031	2.40	5.38
134.684±0.008	2.423±0.296	0.029±0.009	53.22	850.27
135.676±0.003	2.14±0.64	0.005±0.003		696.83
139.016±0.012	2.537±0.235	0.053±0.013	41.40	828.53
140.666±0.011	3.487±0.321	0.05±0.011	88.63	1811.53
142.994±0.012	1.377±0.163	0.039±0.013	13.06	200.27
143.242±0.004	0.596±0.216	0.005±0.006	5.86	22.43
146.333±0.003	2.991±0.723	0.007±0.004		854.97
146.58±0.185	1.097±0.23	0.4±0.237	3.02	9.11
147.368±0.009	3.069±0.348	0.033±0.009	83.67	1190.76
147.847±0.008	0.346±0.152	0.005±0.009	2.69	0.79
148.696±0.012	1.183±0.155	0.037±0.016	11.26	127.76
149.417±0.004	0.38±0.162	0.005±0.007	2.83	5.40
150.061±0.005	0.377±0.148	0.005±0.009	2.21	7.23
151.259±0.009	2.077±0.268	0.028±0.01	40.21	378.80
151.567±0.01	1.963±0.231	0.036±0.012	31.52	322.33
153.169±0.012	3.306±0.281	0.06±0.013	70.61	1570.04
155.625±0.021	1.084±0.129	0.068±0.026	6.36	86.11
155.981±0.009	0.439±0.131	0.011±0.01	3.25	6.30
157.84±0.021	0.915±0.136	0.059±0.034	4.87	54.62
159.361±0.014	2.106±0.19	0.061±0.015	27.23	537.51
160.552±0.01	1.699±0.209	0.031±0.01	24.64	345.42
164.184±0.041	2.141±0.128	0.243±0.041	12.97	353.79
165.86±0.023	2.28±0.156	0.129±0.026	21.13	494.73
168.477±0.079	0.752±0.146	0.178±0.108	2.60	11.50
170.943±0.012	1.106±0.149	0.032±0.012	10.69	121.79
172.419±0.025	1.447±0.126	0.101±0.025	10.38	180.14
174.011±0.02	0.606±0.122	0.033±0.02	3.29	18.39
176.354±0.054	0.495±0.166	0.041±0.059	2.15	3.71
177.191±0.083	1.117±0.133	0.262±0.091	2.46	40.79
178.721±0.078	1.367±0.137	0.357±0.12	3.32	74.91
185.387±0.04	0.826±0.117	0.105±0.043	3.45	30.61
189.817±0.065	0.703±0.13	0.14±0.077	2.52	12.14
192.718±0.05	0.618±0.15	0.106±0.092	1.49	8.13

Table B27. Resolved oscillations for KIC 10200377 .

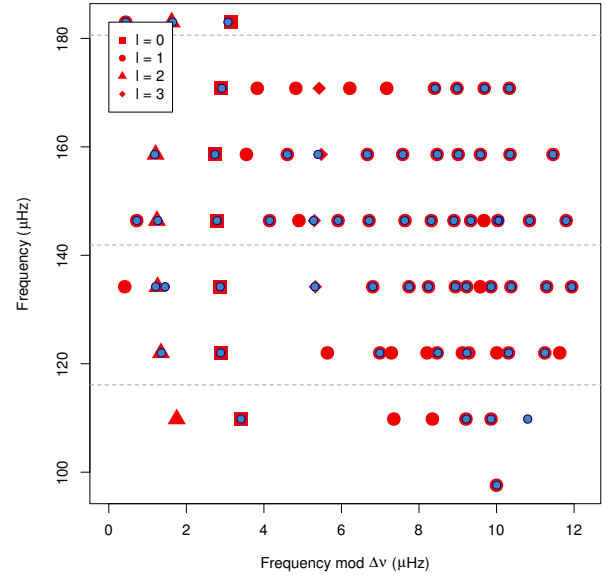
ν_k	H_k	AIC
108.856±0.002	55.79±32.438	41.14
121.649±0.002	93.282±58.418	67.63
132.384±0.002	22.15±14.244	24.95
137.025±0.002	68.52±43.003	79.00
138.529±0.002	138.229±75.43	84.18
139.512±0.002	35.226±28.378	36.92
140.054±0.002	33.989±29.921	30.67
144.859±0.001	172.249±110.713	276.67
150.399±0.001	166.524±132.412	126.34
152.199±0.002	76.12±49.178	57.73
152.496±0.002	22.868±21.707	17.25
162.361±0.002	63.45±38.877	60.74

Table B28. Unresolved oscillations for KIC 10200377 .**Figure B14.** Same as Fig. 14 for KIC 10200377.

ν_k	A_k	γ_k	SNR	AIC
107.603±0.025	0.529±0.113	0.039±0.023	2.86	9.97
113.211±0.041	0.661±0.112	0.073±0.032	2.75	16.56
119.019±0.013	0.839±0.131	0.032±0.016	5.55	59.45
119.657±0.01	0.899±0.149	0.021±0.01	8.26	83.19
120.603±0.01	0.385±0.118	0.011±0.01	2.24	5.28
123.358±0.024	0.905±0.121	0.066±0.029	4.72	53.98
124.884±0.018	1.348±0.134	0.067±0.019	10.85	176.92
131.234±0.022	1.412±0.129	0.086±0.022	7.18	183.76
132.311±0.004	0.849±0.229	0.006±0.004		92.61
135.407±0.01	1.605±0.193	0.034±0.011	20.05	305.30
135.651±0.009	0.651±0.155	0.014±0.011	5.71	19.52
137.073±0.014	2.101±0.186	0.062±0.015	26.34	557.82
139.517±0.014	0.805±0.126	0.031±0.014	5.72	51.70
141.945±0.003	1.182±0.376	0.005±0.004	23.03	181.24
142.445±0.004	1.224±0.283	0.008±0.005	24.05	188.94
143.138±0.011	1.866±0.217	0.037±0.012	24.07	316.54
143.422±0.009	1.775±0.241	0.027±0.01	31.03	259.84
144.059±0.005	1.509±0.287	0.012±0.005	30.13	295.07
147.664±0.017	2.812±0.2	0.095±0.019	37.51	957.05
149.19±0.009	3.7±0.398	0.036±0.009	106.77	2007.43
151.683±0.017	1.112±0.131	0.053±0.018	8.32	105.48
153.112±0.002	1.222±0.322	0.005±0.004		329.91
154.032±0.005	0.98±0.236	0.007±0.004	17.46	125.23
154.714±0.004	2.062±0.424	0.009±0.004	71.31	612.21
155.302±0.008	1.87±0.258	0.024±0.009	34.59	374.60
155.738±0.007	2.383±0.322	0.023±0.008	57.43	718.59
156.432±0.007	1.253±0.223	0.016±0.008		153.82
157.255±0.011	0.459±0.122	0.014±0.01	3.15	9.01
159.785±0.021	2.829±0.18	0.128±0.023	33.23	912.07
161.338±0.015	2.673±0.21	0.077±0.016	38.52	830.92
163.995±0.006	0.31±0.15	0.005±0.012	1.79	3.13
167.075±0.017	1.28±0.142	0.058±0.019	9.69	133.40
167.617±0.019	1.284±0.139	0.065±0.021	8.90	123.85
168.184±0.017	1.029±0.135	0.048±0.019	7.05	76.38
168.949±0.006	0.627±0.159	0.009±0.006	6.46	34.98
172.223±0.044	1.596±0.119	0.202±0.041	8.27	169.28
173.714±0.035	1.56±0.124	0.162±0.038	8.74	171.95
179.218±0.034	0.555±0.142	0.057±0.05	1.99	6.35
179.786±0.02	1.203±0.13	0.072±0.024	7.85	115.07
180.493±0.047	0.745±0.126	0.102±0.049	2.31	17.35
181.129±0.02	0.531±0.121	0.034±0.024	2.74	9.60
183.436±0.013	0.351±0.121	0.012±0.012	1.85	2.19
184.642±0.053	0.792±0.136	0.131±0.075	2.38	20.26
186.073±0.093	0.992±0.136	0.265±0.115	2.48	30.51
197.678±0.117	0.689±0.185	0.219±0.202	1.45	6.18

Table B29. Resolved oscillations for KIC 10257278 .

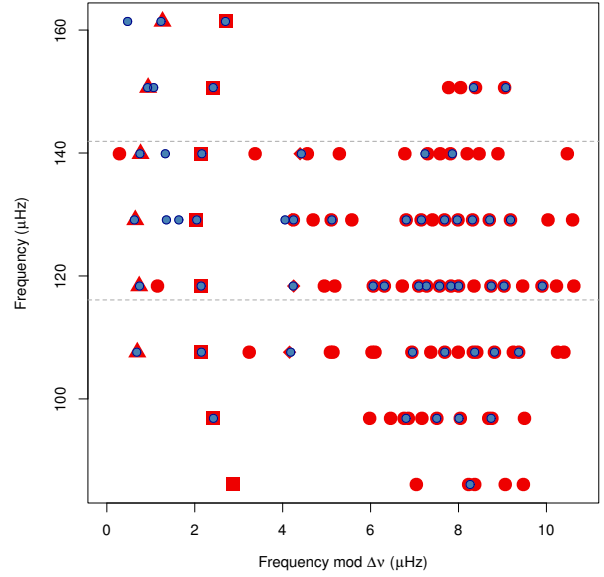
ν_k	H_k	AIC
128.989±0.002	31.395±19.874	25.95
130.487±0.002	76.194±46.358	50.92
133.246±0.002	25.07±17.63	29.03
141.006±0.002	80.675±88.066	140.31
144.578±0.001	26.934±20.047	34.64
145.492±0.002	22.57±17.844	25.24
146.141±0.001	57.948±37.929	74.29
150.548±0.002	22.209±19.329	26.91
152.312±0.001	41.453±37.006	67.27
158.193±0.002	59.328±33.223	35.50
163.205±0.002	30.553±19.126	37.07
165.266±0.002	22.45±21.499	28.07
166.178±0.002	27.108±19.989	28.98
170.055±0.002	22.437±15.358	21.06

Table B30. Unresolved oscillations for KIC 10257278 .**Figure B15.** Same as Fig. 14 for KIC 10257278.

ν_k	A_k	γ_k	SNR	AIC
94.344±0.043	0.801±0.129	0.11±0.061	2.64	26.67
99.265±0.029	1.108±0.117	0.096±0.029	6.45	87.31
103.647±0.025	0.706±0.113	0.042±0.016	4.97	28.46
104.345±0.013	0.993±0.138	0.034±0.013	8.62	86.13
104.852±0.014	1.085±0.142	0.039±0.016	9.16	107.74
105.581±0.023	0.651±0.122	0.036±0.022	3.72	22.83
108.281±0.026	1.172±0.125	0.095±0.034	6.55	99.25
109.751±0.012	1.934±0.197	0.046±0.013	26.34	481.60
111.782±0.025	0.509±0.132	0.034±0.032	2.23	8.70
114.554±0.027	0.949±0.128	0.085±0.04	4.40	50.13
115.287±0.01	1.707±0.205	0.033±0.011	25.33	346.72
115.968±0.01	1.348±0.179	0.028±0.01	16.88	196.90
116.418±0.004	0.451±0.174	0.005±0.01	3.56	12.35
116.968±0.003	0.605±0.174	0.005±0.006	6.09	63.15
119.104±0.023	2.125±0.149	0.124±0.025	19.95	445.91
120.504±0.012	2.964±0.265	0.054±0.012	56.48	1160.18
122.6±0.021	1.054±0.126	0.059±0.019	7.71	82.88
124.417±0.007	0.714±0.171	0.009±0.006	8.08	43.72
124.673±0.003	1.258±0.357	0.006±0.004	26.73	179.18
125.457±0.006	1.726±0.776	0.007±0.009	37.35	37.41
125.629±0.018	2.505±0.204	0.09±0.024	41.77	516.77
126.187±0.007	1.787±0.306	0.016±0.008	37.63	154.90
126.363±0.011	1.756±0.234	0.032±0.014	24.92	183.30
127.106±0.006	0.736±0.179	0.008±0.004	9.58	48.24
128.267±0.011	0.44±0.128	0.012±0.009	2.96	5.71
129.748±0.024	2.865±0.169	0.16±0.028	29.54	862.42
130.475±0.006	0.55±0.196	0.006±0.008	5.59	7.15
130.757±0.009	0.617±0.187	0.012±0.013	5.00	6.66
131.165±0.01	3.443±0.347	0.041±0.011	90.78	1491.78
133.174±0.013	0.435±0.138	0.013±0.012	2.43	3.76
133.367±0.011	0.973±0.153	0.031±0.019	8.87	79.99
134.239±0.009	0.41±0.124	0.009±0.007	3.22	7.80
136.276±0.011	1.53±0.195	0.033±0.012	14.68	220.25
136.804±0.013	1.51±0.18	0.042±0.016	16.97	169.38
137.092±0.021	1.243±0.158	0.062±0.024	6.07	78.60
137.436±0.009	0.622±0.163	0.014±0.015	4.92	17.34
137.83±0.004	0.483±0.178	0.005±0.01	3.62	21.42
138.304±0.006	0.345±0.16	0.005±0.007	2.16	5.14
140.633±0.03	2.018±0.145	0.175±0.044	12.77	311.39
141.21±0.06	0.64±0.206	0.062±0.065	2.04	1.66
142.041±0.025	2.113±0.147	0.14±0.03	17.31	387.19
144.304±0.025	0.688±0.143	0.048±0.039	3.48	20.57
147.118±0.14	1.344±0.169	0.375±0.125	6.04	35.81
147.739±0.061	1.606±0.145	0.252±0.068	5.16	93.84
151.567±0.061	1.605±0.127	0.334±0.09	3.94	128.16
153.059±0.049	1.215±0.128	0.173±0.057	4.95	69.20
158.981±0.212	0.981±0.152	0.4±0.19	2.17	19.24
161.872±0.062	0.505±0.139	0.068±0.057	1.67	2.10
162.632±0.104	0.819±0.136	0.211±0.097	1.80	14.93
164.098±0.187	0.884±0.163	0.375±0.207	1.29	12.11
174.894±0.031	0.436±0.113	0.035±0.023	1.88	3.27

Table B31. Resolved oscillations for KIC 11353313 .

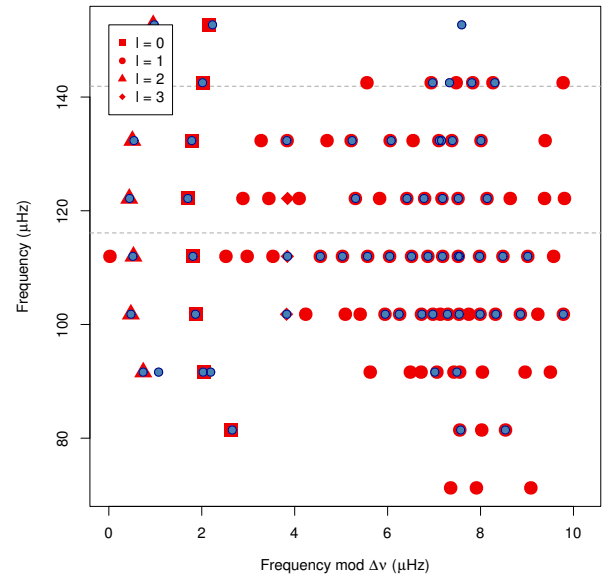
ν_k	H_k	AIC
125.929±0.002	52.115±44.343	15.65
127.395±0.002	43.174±31.602	40.18
135.931±0.001	509.74±267.253	262.75

Table B32. Unresolved oscillations for KIC 11353313 .**Figure B16.** Same as Fig. 14 for KIC 11353313.

ν_k	A_k	γ_k	SNR	AIC
84.097±0.032	0.576±0.114	0.054±0.029	2.54	11.45
89.012±0.03	0.617±0.122	0.062±0.039	2.76	13.93
89.974±0.015	0.397±0.112	0.017±0.012	2.17	4.26
92.358±0.014	1.127±0.14	0.04±0.014	9.30	126.34
92.691±0.013	0.454±0.123	0.015±0.011	2.96	7.29
93.649±0.012	0.751±0.145	0.022±0.017	6.47	42.76
93.811±0.014	0.566±0.126	0.022±0.014	2.98	14.41
98.636±0.026	1.237±0.136	0.092±0.036	7.50	104.40
99.111±0.028	1.036±0.126	0.073±0.023	6.28	60.04
102.276±0.013	1.463±0.16	0.048±0.017	16.88	236.14
103.665±0.012	1.95±0.2	0.045±0.012	26.73	492.32
105.628±0.016	0.595±0.117	0.029±0.016	3.42	19.56
107.749±0.007	0.465±0.135	0.008±0.006	4.30	13.73
108.048±0.015	0.595±0.124	0.021±0.012	4.31	20.92
108.536±0.006	1.188±0.233	0.012±0.006	7.91	158.32
109.088±0.015	1.459±0.171	0.05±0.022	17.95	187.92
109.341±0.006	1.234±0.237	0.012±0.006	21.08	127.24
109.79±0.005	1.013±0.25	0.008±0.005	16.06	120.33
112.498±0.013	2.534±0.222	0.06±0.014	39.13	806.81
113.79±0.008	3.569±0.413	0.033±0.009	111.32	1864.77
115.826±0.022	0.888±0.125	0.062±0.029	4.65	49.16
116.533±0.004	0.342±0.127	0.005±0.006	4.00	11.15
117.546±0.004	1.14±0.261	0.006±0.003		187.74
118.495±0.004	2.322±0.515	0.009±0.004	40.26	739.39
118.848±0.006	1.811±0.314	0.015±0.007		358.70
119.499±0.006	1.887±0.364	0.012±0.007		358.26
119.96±0.006	0.93±0.192	0.012±0.007		87.46
122.606±0.015	3.024±0.231	0.079±0.017	88.62	1117.60
123.86±0.011	3.47±0.318	0.051±0.012	3.66	1600.53
128.577±0.008	1.311±0.216	0.02±0.01		139.12
128.943±0.02	1.462±0.163	0.071±0.028	14.56	141.17
129.344±0.011	1.635±0.202	0.035±0.012	20.55	215.08
129.681±0.014	1.024±0.152	0.034±0.014	8.47	64.64
130.304±0.014	0.653±0.129	0.024±0.014	4.49	25.39
132.88±0.045	1.572±0.126	0.218±0.056	6.77	147.51
134.125±0.018	2.094±0.166	0.09±0.021	21.34	446.89
136.172±0.004	0.363±0.13	0.005±0.007	1.87	11.07
137.576±0.004	0.387±0.153	0.005±0.008	3.05	9.68
138.417±0.005	0.374±0.149	0.005±0.007	2.83	7.54
139.452±0.017	0.78±0.125	0.045±0.014	3.94	5.71
139.499±0.114	1.278±0.164	0.318±0.129	3.78	22.91
139.734±0.024	0.947±0.151	0.058±0.019	2.63	7.51
143.279±0.094	1.035±0.138	0.249±0.101	2.36	34.41
144.537±0.04	1.213±0.124	0.149±0.049	5.19	84.31
149.488±0.048	0.695±0.137	0.109±0.069	1.57	12.96
149.851±0.034	0.442±0.14	0.039±0.038	1.71	0.95
150.332±0.044	0.598±0.148	0.086±0.072	1.38	7.04
150.826±0.03	0.528±0.12	0.046±0.028	1.96	6.93
153.678±0.081	1.244±0.127	0.324±0.102	3.14	61.22
154.932±0.045	0.713±0.149	0.104±0.076	1.98	13.67
160.295±0.015	0.557±0.118	0.025±0.017	3.20	17.08

Table B33. Resolved oscillations for KIC 11913545 .

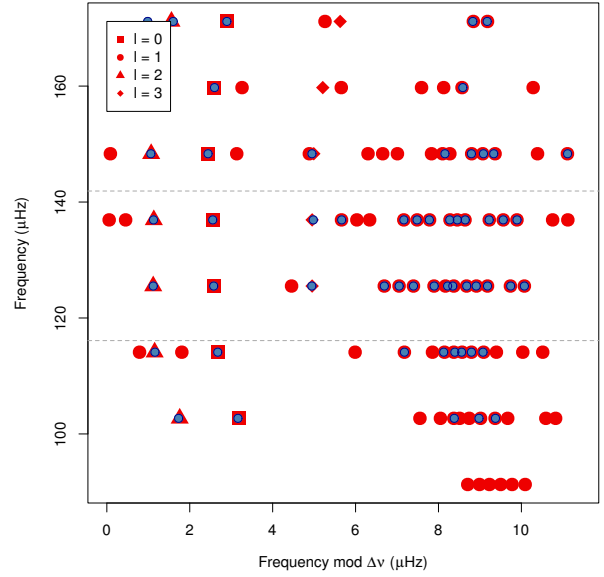
ν_k	H_k	AIC
108.773±0.002	371.821±242.555	92.18
110.129±0.001	65.433±43.77	59.16
110.66±0.001	39.651±27.856	71.86
111.581±0.001	35.493±36.682	46.76
117.009±0.001	92.303±40.359	175.35
118.024±0.001	48.979±26.489	84.12
119.159±0.001	1469.197±534.294	391.85
120.462±0.001	106.578±73.478	134.75
120.996±0.001	67.169±31.529	101.84
127.471±0.002	40.57±34.03	54.41

Table B34. Unresolved oscillations for KIC 11913545 .**Figure B17.** Same as Fig. 14 for KIC 11913545.

ν_k	A_k	γ_k	SNR	AIC
104.421±0.026	0.598±0.111	0.044±0.021	3.32	15.80
105.853±0.029	0.658±0.114	0.057±0.027	3.18	19.47
111.071±0.018	0.464±0.118	0.024±0.018	2.33	6.37
111.668±0.065	0.775±0.15	0.125±0.086	2.48	20.19
112.064±0.009	0.487±0.137	0.011±0.01	3.88	12.89
115.261±0.026	1.033±0.12	0.08±0.029	5.08	75.94
116.775±0.019	1.06±0.124	0.056±0.018	7.75	94.83
121.279±0.004	0.405±0.158	0.005±0.006	3.60	10.92
122.226±0.016	0.648±0.13	0.034±0.024	2.94	21.37
122.495±0.011	0.864±0.146	0.025±0.014	3.71	62.73
122.658±0.008	0.493±0.175	0.007±0.009	7.05	14.50
123.174±0.012	0.485±0.119	0.016±0.01	3.40	11.99
126.629±0.019	1.748±0.149	0.081±0.019	16.45	314.67
128.088±0.017	2.013±0.164	0.08±0.018	21.34	457.96
130.455±0.023	0.643±0.117	0.038±0.02	4.47	21.70
133.73±0.023	1.922±0.152	0.104±0.025	12.55	355.84
134.42±0.006	1.307±0.245	0.013±0.007	10.07	167.18
135.252±0.008	0.565±0.14	0.01±0.006	5.35	24.12
135.582±0.004	0.463±0.181	0.005±0.009	4.29	28.48
138.046±0.015	2.668±0.204	0.081±0.017	37.82	882.53
139.475±0.008	3.505±0.402	0.031±0.009	106.78	1833.51
141.9±0.037	0.739±0.125	0.069±0.039	3.45	24.44
144.403±0.007	1.076±0.2	0.015±0.008	14.96	116.36
144.7±0.005	1.597±0.312	0.011±0.005	34.38	310.92
145.191±0.007	1.611±0.283	0.016±0.007	26.70	159.26
145.375±0.006	2.473±0.395	0.017±0.007	67.25	553.26
145.566±0.005	1.589±0.342	0.009±0.005	38.41	177.51
146.482±0.005	0.571±0.172	0.006±0.005	6.19	28.00
149.392±0.022	2.749±0.171	0.14±0.025	29.64	824.56
150.772±0.018	2.264±0.177	0.089±0.02	25.99	508.27
153.278±0.028	0.735±0.116	0.05±0.021	4.51	28.18
156.486±0.035	1.906±0.13	0.209±0.048	10.05	288.17
157.415±0.015	0.926±0.142	0.037±0.017	6.34	49.96
157.663±0.02	0.434±0.14	0.022±0.022	1.53	1.28
159.444±0.006	0.329±0.136	0.005±0.006	2.93	5.30
161.027±0.054	1.499±0.121	0.245±0.058	5.68	124.98
162.337±0.028	1.488±0.13	0.12±0.032	9.15	163.17
168.327±0.051	1.269±0.12	0.208±0.063	5.38	88.73
172.136±0.048	0.55±0.144	0.086±0.074	1.48	4.43
172.751±0.013	0.738±0.135	0.026±0.016	5.17	40.78
174.045±0.039	1.1±0.124	0.146±0.057	4.35	67.74
179.978±0.045	0.623±0.123	0.081±0.046	1.51	10.86
180.325±0.019	0.487±0.141	0.02±0.024	2.73	9.67
184.557±0.003	0.293±0.077	0.01±NaN	2.01	3.91

Table B35. Resolved oscillations for KIC 11968334 .

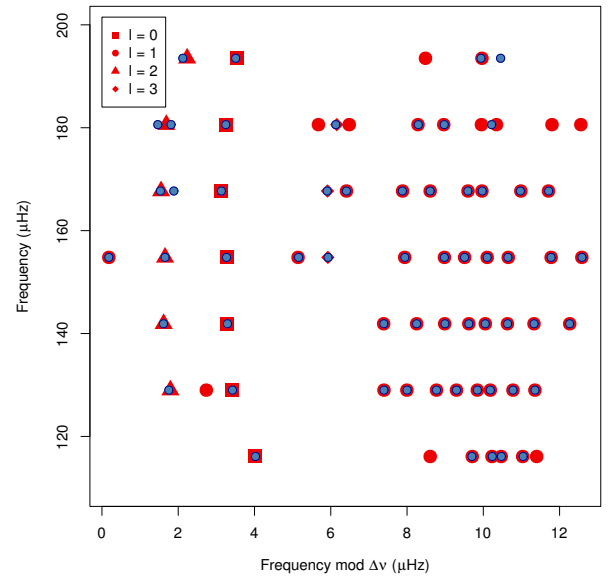
ν_k	H_k	AIC
122.895±0.002	66.213±45.672	68.73
132.204±0.002	38.296±19.552	62.24
132.562±0.001	92.73±80.836	138.46
132.906±0.002	42.868±22.898	65.58
133.406±0.002	61.114±51.565	38.05
133.856±0.004	38.933±44.564	3.61
134.191±0.002	304.135±168.703	44.08
134.693±0.001	195.375±100.549	158.83
142.585±0.001	40.139±27.954	66.26
144.085±0.001	123.51±73.516	150.67
146.143±0.002	151.484±79.545	104.09
146.814±0.002	34.801±20.522	43.84

Table B36. Unresolved oscillations for KIC 11968334 .**Figure B18.** Same as Fig. 14 for KIC 11968334.

ν_k	A_k	γ_k	SNR	AIC
120.126±0.019	0.758±0.117	0.044±0.02	4.17	38.49
125.802±0.017	0.463±0.116	0.025±0.018	2.38	7.31
126.334±0.014	0.529±0.12	0.019±0.011	3.60	13.88
126.573±0.017	0.727±0.119	0.035±0.015	4.18	35.40
127.146±0.005	0.416±0.182	0.005±0.008	3.71	16.11
130.754±0.051	0.845±0.118	0.132±0.052	3.40	28.24
132.422±0.014	1.328±0.15	0.045±0.015	12.10	191.02
136.395±0.005	0.595±0.173	0.007±0.007	5.96	37.58
137.771±0.005	0.428±0.144	0.005±0.004	3.28	16.68
138.844±0.009	1.125±0.172	0.022±0.009	12.70	132.35
139.182±0.011	1.08±0.151	0.031±0.012	9.89	111.48
143.513±0.015	1.629±0.157	0.06±0.016	16.72	294.61
145.191±0.012	2.208±0.215	0.049±0.013	35.47	659.07
149.292±0.004	0.366±0.123	0.005±0.006	2.38	13.37
150.894±0.006	0.899±0.184	0.012±0.007	10.87	86.59
151.521±0.006	2.356±0.394	0.014±0.006	83.04	795.54
151.95±0.008	1.734±0.247	0.022±0.009	30.86	355.22
152.536±0.009	1.071±0.17	0.022±0.01	11.91	117.22
153.231±0.006	0.951±0.198	0.011±0.007	12.97	106.41
156.455±0.02	2.31±0.165	0.106±0.021	24.76	592.69
158.065±0.009	3.429±0.373	0.035±0.009	90.77	1765.53
159.956±0.01	0.605±0.13	0.018±0.011	4.12	24.14
160.726±0.026	0.9±0.116	0.062±0.021	5.81	52.78
162.743±0.005	0.765±0.2	0.008±0.006	9.55	64.90
163.778±0.005	1.774±0.349	0.011±0.005	43.34	403.30
164.308±0.012	1.781±0.193	0.044±0.015	25.30	330.97
164.902±0.007	2.342±0.322	0.023±0.008	61.51	709.82
165.445±0.005	1.677±0.349	0.01±0.005	40.27	363.54
167.386±0.005	0.453±0.161	0.005±0.005	4.39	17.24
169.211±0.018	2.67±0.193	0.095±0.019	35.18	821.39
170.83±0.01	3.07±0.321	0.039±0.01	67.51	1335.38
173.614±0.053	0.69±0.118	0.094±0.042	1.92	15.03
174.111±0.003	0.552±0.195	0.005±0.008	5.67	31.59
176.303±0.003	1.402±0.395	0.005±0.003		285.23
177.295±0.014	1.433±0.164	0.045±0.014	13.60	176.47
177.671±0.012	1.563±0.18	0.04±0.014	18.64	232.89
179.413±0.008	0.567±0.134	0.013±0.01	4.35	23.89
182.07±0.02	1.137±0.138	0.062±0.023	6.15	86.76
182.414±0.012	1.238±0.169	0.031±0.011	12.86	127.48
183.848±0.024	1.917±0.139	0.122±0.025	15.82	368.27
186.736±0.037	0.582±0.129	0.05±0.038	2.68	11.83
188.895±0.015	0.632±0.12	0.026±0.013	4.59	23.97
189.575±0.013	0.806±0.134	0.028±0.013	6.26	47.79
190.813±0.041	1.678±0.119	0.184±0.036	10.45	220.47
195.625±0.099	1.295±0.126	0.379±0.104	2.42	61.07
197.017±0.04	1.134±0.121	0.135±0.042	5.06	67.60
203.439±0.044	0.689±0.121	0.092±0.046	2.05	15.45
203.953±0.034	0.568±0.123	0.051±0.034	2.23	9.69
208.388±0.018	0.479±0.119	0.027±0.02	2.20	7.81
209.086±0.082	0.559±0.14	0.123±0.084	1.17	2.75
210.56±0.052	0.712±0.145	0.125±0.091	2.16	14.27

Table B37. Resolved oscillations for KIC 12008916 .

ν_k	H_k	AIC
138.297±0.001	42.283±38.461	49.67
139.777±0.002	28.635±24.084	24.74
150.157±0.001	291.229±202.156	320.05
154.164±0.001	42.179±33.057	61.94
154.981±0.001	64.75±36.938	90.01
166.578±0.002	81.346±44.237	91.20
169.582±0.002	374.07±199.403	59.65
175.577±0.002	161.837±76.891	128.42
176.347±0.002	24.322±23.96	5.27
178.679±0.002	108.316±68.092	67.41

Table B38. Unresolved oscillations for KIC 12008916 .**Figure B19.** Same as Fig. 14 repeated here for completeness.

This paper has been typeset from a \TeX/L\AA\TeX file prepared by the author.